Resource

Cell Reports

A Mass Spectrometry-Based Approach for Mapping Protein Subcellular Localization Reveals the Spatial Proteome of Mouse Primary Neurons

Graphical Abstract

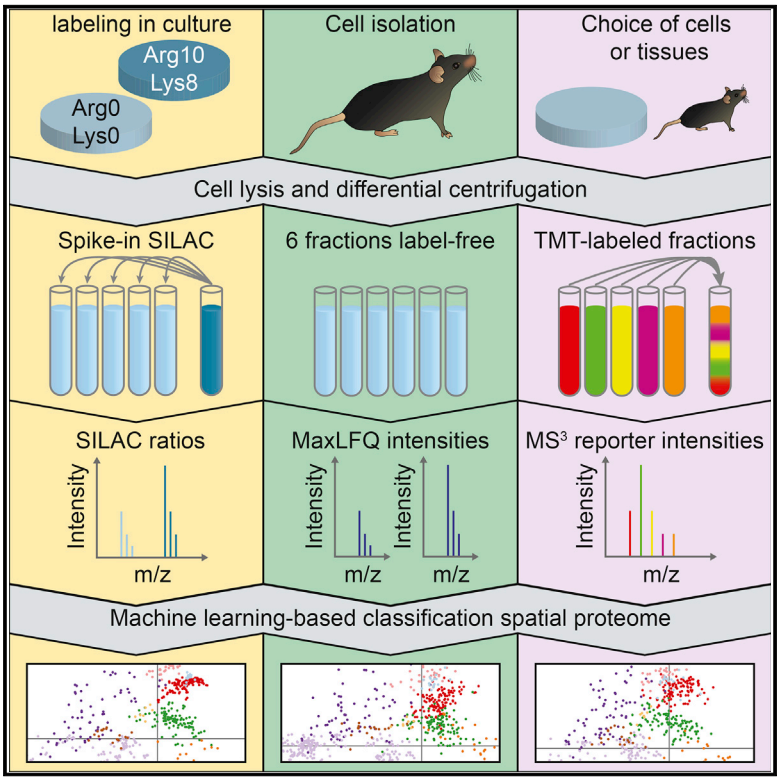

Highlights

- High-resolution organellar maps with label-free quantification (LFQ)
- High-throughput organellar maps with TMT-based multiplexing
- Deep mapping of EGF-induced protein localization changes with SILAC, LFQ, and TMT
- A quantitative spatial proteome from mouse primary neurons

Authors

Daniel N. Itzhak, Colin Davies, Stefka Tyanova, ..., Jürgen Cox, Michael P. Weekes, Georg H.H. Borner

Correspondence

borner@biochem.mpg.de

In Brief

Dynamic organellar maps previously provided a proteomic method for capturing protein subcellular localization changes in cultured cells. Itzhak et al. have now adapted the approach to a universal format, extending the method to all cell types. Application to primary mouse neurons provides spatial and quantitative information for more than 8,000 proteins.

Itzhak et al., 2017, Cell Reports *20*, 2706–2718
September 12, 2017
http://dx.doi.org/10.1016/j.celrep.2017.08.063

CellPress

OPEN ACCESS
CellPress

Cell Reports
Resource

A Mass Spectrometry-Based Approach for Mapping Protein Subcellular Localization Reveals the Spatial Proteome of Mouse Primary Neurons

Daniel N. Itzhak,[1] Colin Davies,[2] Stefka Tyanova,[1] Archana Mishra,[3] James Williamson,[2] Robin Antrobus,[2] Jürgen Cox,[1] Michael P. Weekes,[2,4] and Georg H.H. Borner[1,4,5,*]

[1]Department of Proteomics and Signal Transduction, Max Planck Institute of Biochemistry, 82152 Martinsried, Germany
[2]Cambridge Institute for Medical Research, University of Cambridge, Hills Road, Cambridge CB2 0XY, UK
[3]Department of Molecules-Signaling-Development, Max Planck Institute of Neurobiology, 82152 Martinsried, Germany
[4]Senior author
[5]Lead Contact
*Correspondence: borner@biochem.mpg.de
http://dx.doi.org/10.1016/j.celrep.2017.08.063

SUMMARY

We previously developed a mass spectrometry-based method, dynamic organellar maps, for the determination of protein subcellular localization and identification of translocation events in comparative experiments. The use of metabolic labeling for quantification (stable isotope labeling by amino acids in cell culture [SILAC]) renders the method best suited to cells grown in culture. Here, we have adapted the workflow to both label-free quantification (LFQ) and chemical labeling/multiplexing strategies (tandem mass tagging [TMT]). Both methods are highly effective for the generation of organellar maps and capture of protein translocations. Furthermore, application of label-free organellar mapping to acutely isolated mouse primary neurons provided subcellular localization and copy-number information for over 8,000 proteins, allowing a detailed analysis of organellar organization. Our study extends the scope of dynamic organellar maps to any cell type or tissue and also to high-throughput screening.

INTRODUCTION

Spatial proteomics is an emerging field that promises to chart the location of all proteins within cells, allowing a systems view of cellular organization (Boisvert et al., 2012; Christoforou et al., 2016; Foster et al., 2006; Hesketh et al., 2017; Itzhak et al., 2016; Jadot et al., 2017; Jean Beltran et al., 2016; Mardakheh et al., 2016; Rhee et al., 2013; Weekes et al., 2014; reviewed in Aebersold and Mann, 2016; Drissi et al., 2013; Jean Beltran et al., 2017; Larance and Lamond, 2015). We have previously developed a profiling method for the generation of highly reproducible organellar maps (Itzhak et al., 2016) that also allows dynamic mapping of induced changes in protein localization. The method combines rapid subcellular fractionation with quantitative mass spectrometry (MS). Because it relies on metabolic labeling (stable isotope labeling by amino acids in cell culture [SILAC]; Ong et al., 2002) for profile quantification, it is mostly suited to cells in culture. To expand the range of applications, here we have developed workflows for label-free quantification using MaxLFQ (Cox et al., 2014) and tandem mass tag (TMT)-based quantification using the MS3/multi-notch approach (McAlister et al., 2012, 2014). We provide a comparison of the advantages of each method for generating dynamic organellar maps and apply the label-free workflow to neurons, deriving a high-resolution quantitative spatial proteome from primary cells.

RESULTS AND DISCUSSION

Adaptation of the Dynamic Organellar Maps Workflow

The principle of subcellular proteomic profiling is to partially separate organelles by biochemical means and then to quantify the distributions of proteins across the differentially enriched subfractions. Organelle-specific profiles are derived from the distributions of known marker proteins, enabling subcellular assignment of proteins without known location. Importantly, complete isolation of individual organelles is not required; overlapping profiles can be de-convoluted and resolved by subsequent cluster analysis, provided they are sufficiently different. In the original dynamic organellar maps workflow, cell lysate is separated by differential centrifugation into six fractions (Itzhak et al., 2016). Each of the five post-nuclear pellets is mixed 1:1 with a SILAC heavy "reference" membrane fraction, followed by MS analysis (Figure 1A). Quantification of heavy to light ratios in each fraction yields abundance profiles across the gradient. For label-free quantification (LFQ) implementation, the SILAC workflow was replicated, omitting the heavy-labeled reference (Figure 1B, left). Profiling was then achieved by direct comparison of protein intensities across fractions using the MaxLFQ algorithm for quantification (Cox et al., 2014). With a five-fraction workflow (LFQ5), some organelles showed overlapping profiles. Inclusion of the sixth (nuclear-enriched) fraction (LFQ6) and re-normalization substantially enhanced the resolution of these profiles (Figure 1B, center and right). For a chemical labeling profiling approach, following fractionation and protein digestion, peptides were conjugated with TMT reagent (McAlister et al., 2012, 2014). Each tag has the same mass but, upon fragmentation, gives rise to reporter ions with different masses; these are

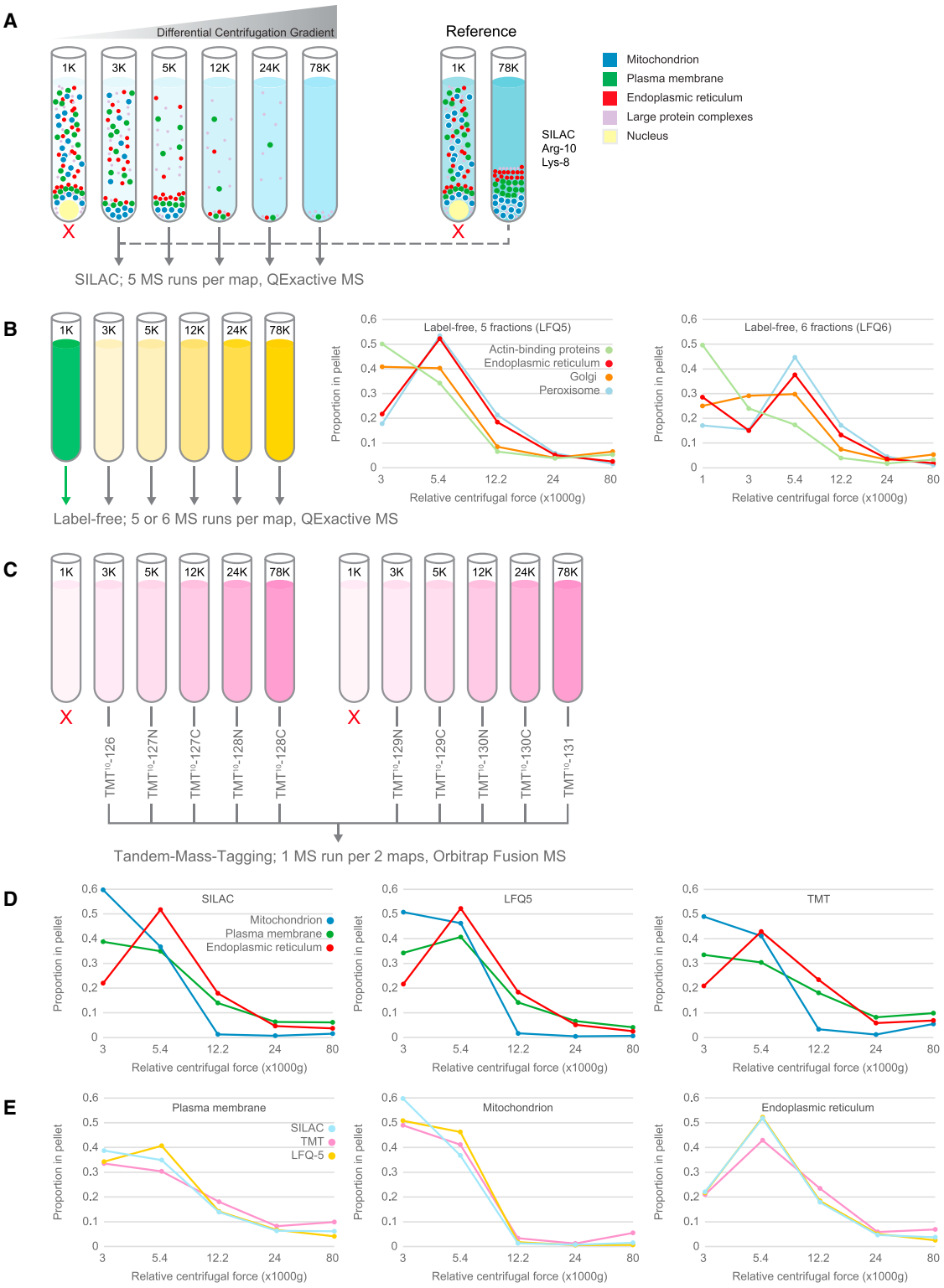

Figure 1. Workflow for Dynamic Organellar Maps Using Fractionation Profiling

(A) In all workflows, whole-cell lysate was subjected to differential centrifugation to generate fractions enriched in different organelles. Note that the nuclear-enriched 1K fraction also contains a proportion of non-nuclear material. For the SILAC workflow, heavy-labeled post-nuclear supernatant was subjected to a single centrifugation step to generate a reference membrane fraction. Each of the fractions, excluding the 1K nuclear fraction, was combined 1:1 with the

(legend continued on next page)

used to quantify the abundance of the parent peptides across samples. For maximum accuracy, reporter ions were analyzed with a synchronous precursor selection MS3 approach to avoid ratio compression effects (McAlister et al., 2014).The recent development of 10-plex TMT enabled combination of two maps of five fractions in a single MS run (Figure 1C). With all three profiling strategies, median profiles of major organelles were clearly resolved (Figure 1D). Furthermore, comparing profiles of the same organelle across methods revealed that they were closely matched (Figure 1E).

Evaluation of SILAC, LFQ, and TMT Map Performance

Map performance for the different quantification strategies was assessed with two MS protocols, a "fast" method that minimizes measuring time and a "deep" method that maximizes protein coverage. These reflect run parameters we anticipate will be employed by users. The MS measurement requirements for SILAC and LFQ5 were identical (12.5 hr/fast map, 37.5 hr/deep map), and substantially lower for TMT (1.5 hr/fast map, 19 hr/deep map) because of the multiplexing of samples.

It was expected that the LFQ implementation would be most challenging because of the noisier quantification relative to SILAC or TMT (Figure 2A); hence, the LFQ approach was optimized most extensively. Six independent LFQ maps were prepared from HeLa cells with the fast MS protocol. Data transformation and quality filtering were adjusted for LFQ profiles as detailed in the Supplemental Experimental Procedures. Organellar predictions were generated using supervised learning (support vector machines [SVMs]) of a set of approximately 1,000 marker proteins covering 12 subcellular localizations (Itzhak et al., 2016). The proportion of accurately assigned markers was scored (global prediction accuracy; Figure 2B). The average map performance for LFQ5 (fast) was 87.3%. Inclusion of the sixth fraction led to a consistent and substantial boost in prediction accuracy, taking performance to an average of 91.1% for LFQ6. For reference, SILAC (fast) maps average ~94% accuracy.

Organellar classification using the combined profiles of several SILAC maps enhances performance (Itzhak et al., 2016). To investigate this effect with LFQ, classification was performed with one to six LFQ (fast) maps, combining them in order of performance from worst to best (Figure 2C). Each additional map improved the performance, plateauing at 5 maps (prediction accuracy, ~94% for LFQ6). Three maps of intermediate performance were selected for more extensive MS analysis (deep protocol). This revealed that two deep LFQ maps combined had equivalent prediction accuracy as five fast maps (Figure 2C). An equivalent analysis was performed for TMT maps (single maps versus a combinations of maps, fast versus deep protocols) as well as for SILAC (to serve as a reference; Figure S1). In all cases, a combination of three maps provided high-accuracy organellar predictions (Figure 2D). Using the deep protocol, SILAC provided the best global prediction accuracy at 97.1%; LFQ5 and TMT maps had slightly lower accuracies (around 91%) but were still very good in absolute terms. The boost from including the extra fraction placed LFQ6 performance close to SILAC (94.7%). The number of profiled proteins was lowest with SILAC (3,700), whereas that with LFQ exceeded 5,500 (Figure 2E). With TMT, 4,500 proteins were profiled; however, two of three replicates covered more than 6,000 proteins, suggesting that the depth should reach that of LFQ maps. The fast protocol provided a slightly lower map accuracy in all cases, but it was still very high for SILAC (95.8%) and LFQ6 (92.4%). TMT fast also had good accuracy (91.3%), although this was calculated for a smaller set of resolved clusters (Figure 2D; Figure S1G). MS measuring time requirements were substantially lower with TMT quantification, especially with the fast protocol (only 4.5 hr/three maps; Figure 2F).

For in-depth performance analysis of maps generated with the different quantification methods, the predictions for individual organellar clusters were evaluated. We calculated recall (the proportion of marker proteins correctly assigned to the cluster) and precision (the proportion of all assignments to this cluster that are correct). A perfectly resolved cluster includes all relevant marker proteins and no markers from any other clusters (recall and precision = 1). The harmonic mean of recall and precision, the F1 score, provides a single metric of cluster performance. A comparison of the different methods revealed that some clusters perform well irrespective of the MS acquisition method (Figure 2G); these included the largest clusters: plasma membrane, mitochondrion, endoplasmic reticulum, and large protein complex as well as endosome, lysosome, and actin-binding proteins. Smaller clusters, including peroxisome, nuclear pore complex, Golgi, and ER-Golgi intermediate compartment (ERGIC), performed less well in TMT and LFQ5 compared with SILAC. The benefit of LFQ6 relative to LFQ5 was also most evident for these clusters. Defining an F1 score of > 0.7 as a well-resolved cluster, both SILAC and LFQ6 resolved all 12 clusters, suggesting that these are the preferred methods for the highest-resolution maps; although not directly tested here, a TMT-based deep analysis with 6 fractions would be likely to yield results similar to LFQ6 (Figure 2G). Figures S1F–S1I show how the F1 scores improve when using the deep protocol compared with the fast protocol.

Organellar predictions of non-marker proteins were stratified into four confidence classes based on SVM scores (high, medium, low, and very low). Marker prediction accuracies within

reference fraction and measured by MS. The SILAC ratios along the gradient generate profiles for each protein. In comparative experiments, the SILAC heavy reference fraction was from cells treated to match the fractionated material.

(B) LFQ workflow. The same differential centrifugation as for SILAC light was used. Including the 1K nuclear-enriched fraction in the analysis increased separation of some organelles, as seen by comparing median organellar marker profiles (5 fractions, center, versus 6 fractions, right). Please note that inclusion of the 6th fraction also entails re-normalization of the profile to a sum of 1; this causes relative shifts in all fractions.

(C) TMT workflow, which used identical fractions as the SILAC light workflow. Following protein digestion, peptides from each fraction were labeled with tandem mass tagging reagent and analyzed on an instrument capable of synchronous precursor selection-MS^3 (SPS-MS3). TMT 10-plex permitted two maps to be measured in a single experiment.

(D) Median profiles for organellar marker proteins are shown for three organelles with the different methods: SILAC (left), LFQ (center), and TMT (right).

(E) As for (D), except profiles for the same organelle obtained with the different quantification strategies are shown.

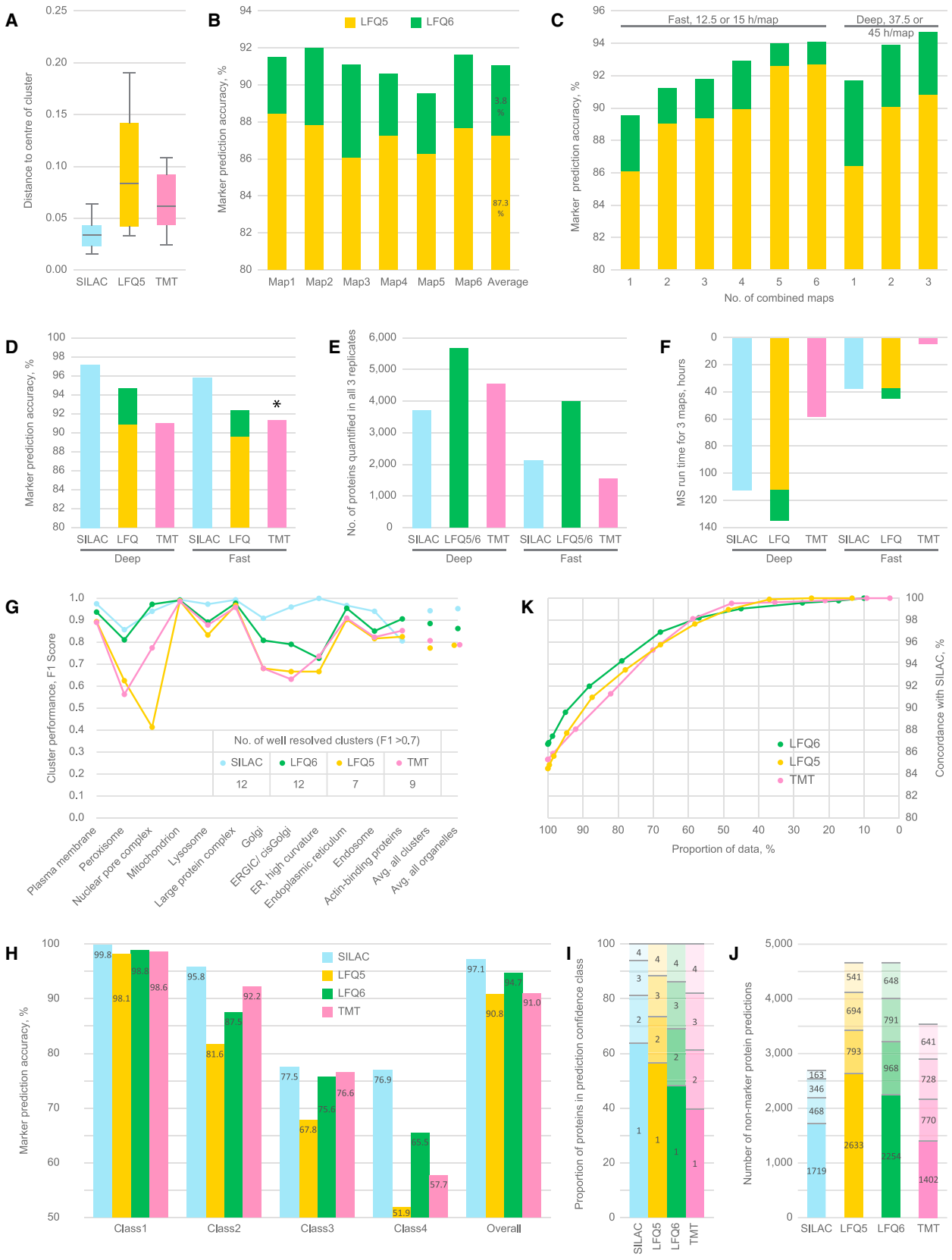

(legend on next page)

each class served as a proxy for the prediction accuracy of non-markers (Figure 2H). SILAC had the greatest proportion of high-confidence predictions, but TMT and LFQ also had high proportions (Figure 2I). Overall, LFQ made the largest number of high-confidence predictions because of the overall number of proteins profiled (Figure 2J; Figures S1C–S1E show the equivalent analyses for maps made with the fast protocol).

Finally, it was evaluated to what extent the organellar assignments made with the different methods agree. Concordance was calculated as the proportion of proteins with identical predictions between two quantification methods. For each comparison, the SILAC (deep) set was used as reference. Importantly, only non-maker predictions were included in the analysis. Baseline concordance was very high in all cases (84%–87%; Figure 2K; Figure S1B). A stringency filter was then applied to restrict comparisons to predictions above a given SVM score. In all cases, concordance reached >96% for the majority of predictions, demonstrating that the three profiling methods yield highly consistent results. Thus, we conclude that the SILAC, LFQ, and TMT quantification strategies are all effective for generating accurate organellar maps.

TMT- and LFQ-Based Dynamic Organellar Maps

We next investigated the suitability of TMT and LFQ maps to capture induced protein translocations. For optimum comparison, an identical set of samples, comprising three replicate experiments of control cells or cells stimulated with epidermal growth factor (EGF) for 20 min, was analyzed with all three methods using both fast and deep protocols. These samples were used previously to follow endocytic uptake of activated EGF receptor (EGFR) but were analyzed only with the fast SILAC protocol (Itzhak et al., 2016). Here, an additional deep MS analysis was performed to determine the full capability of the SILAC approach. To test LFQ maps for dynamic applications, a label-free experiment was simulated by reprocessing the SILAC fast and deep datasets with the MaxLFQ algorithm, ignoring any SILAC heavy-labeled peptides. For TMT dynamic maps, peptides from the SILAC light fractions were TMT-labeled and analyzed by MS (fast and deep protocols).

To identify proteins that show subcellular movement upon EGF treatment, an improved version of our previously developed outlier test was applied (Supplemental Experimental Procedures). This combines metrics for movement distance (M score) and reproducibility (R score) into an "MR" scatterplot analysis. Significantly translocating proteins have both high M and R scores. False discovery rate (FDR) control for cutoff selection was achieved by comparison with a mock experiment (control versus control). These plots revealed that SILAC, TMT, and LFQ implementations of dynamic organellar maps correctly identified the movement of EGFR together with SHC1 and GRB2, two major binding partners of activated EGFR (Figures 3A, 3D, and 3G). The profiles of the EGFR, before and after treatment with EGF (Figures 3B, 3E, and 3H), were remarkably similar across all methods. Furthermore, when subjecting each of the datasets to SVM analysis, all methods correctly classified EGFR as localized to the plasma membrane in control cells and to endosomes in EGF-treated cells (Figures 3C, 3F, and 3I). Importantly, almost identical results were obtained with the corresponding fast analyses (Figure S2), also highlighting the usefulness of all methods in this format.

Although all three approaches successfully identified major translocations, they differed in the number of detected minor movements (Figure S3). Here, SILAC performed best, identifying a total of 66 significant translocations (with an estimated FDR < 10%). 42 of these have previously been linked to EGF signaling, strongly supporting the high predictive value of the analysis; the remaining proteins are hence likely candidate pathway components or downstream targets of EGFR (see Figure S3 and

Figure 2. Performance Analysis of Organellar Maps Generated with TMT, LFQ, and SILAC Quantification Strategies

(A) To illustrate the relative precision of the different quantification methods applied in fractionation profiling, profile scatter within the 20S core proteasome (14 subunits, PSMA1–7, PSMB1–7, three independent measurements per protein) was analyzed (deep MS protocol). LFQ measurements are "noisier" than SILAC or TMT. Boxes indicate the interquartile range and whiskers 10^{th}–90^{th} percentile range.

(B) Organellar classification performance of six independent LFQ-based maps. Accuracy is the proportion of correctly classified organellar markers during supervised learning. Performance was assessed for six-fraction profiles (LFQ6, green) and for the same maps with the sixth data point removed (LFQ5, yellow).

(C) Combining several LFQ maps for organellar classification enhanced prediction accuracy. (Fast) maps shown in (B) were combined in the order of lowest to highest performance. Addition of each map improved performance. Maps 3, 4, and 6 were then chosen for further deep MS analysis and combined for classification.

(D) Marker prediction accuracy obtained with a combination of three replicate maps by quantification strategy and MS protocol. TMT fast maps included predictions for only 10 of 12 clusters (see also Figure S1G).

(E) Number of profiled proteins quantified in all three replicates.

(F) MS measurement requirements (hours) for the generation of three replicate maps.

(G–K) In-depth analysis of the predictions obtained with a combination of three replicate datasets, deep MS protocol (an equivalent analysis for predictions obtained with the fast MS protocol is shown in Figures S1B–S1E).

(G) Detailed performance profiles of maps made with SILAC, LFQ5/6, and TMT. Prediction performance was evaluated for each organellar cluster. F1 scores were calculated as the harmonic mean of recall (true positives / [true positives + false negatives]) and precision (true positives / (true positives + false positives]). High F1 scores (> 0.7) denote clusters with a high predictive value.

(H) Stratification of non-marker organellar predictions. Each assignment was made with a prediction confidence score. Four different SVM score cutoffs were defined, dividing the data into confidence classes. The prediction accuracy of marker proteins within each class served as a proxy for the prediction accuracy of non-marker proteins. Generally, the first two classes had high accuracies with all methods.

(I and J) Proportion (I) and absolute number (J) of non-marker predictions in each confidence class.

(K) Concordance analysis. The predictions of non-marker proteins, obtained with TMT, LFQ5, and LFQ6, were compared with the predictions obtained with SILAC. Concordance is the proportion of proteins with identical predictions. Restricting the comparison to proteins with a minimum confidence score in both compared maps reduces the overlapping dataset but increases concordance. In all cases, over 85% of the predictions show > 90% agreement.

See also Figure S1 and Table S1.

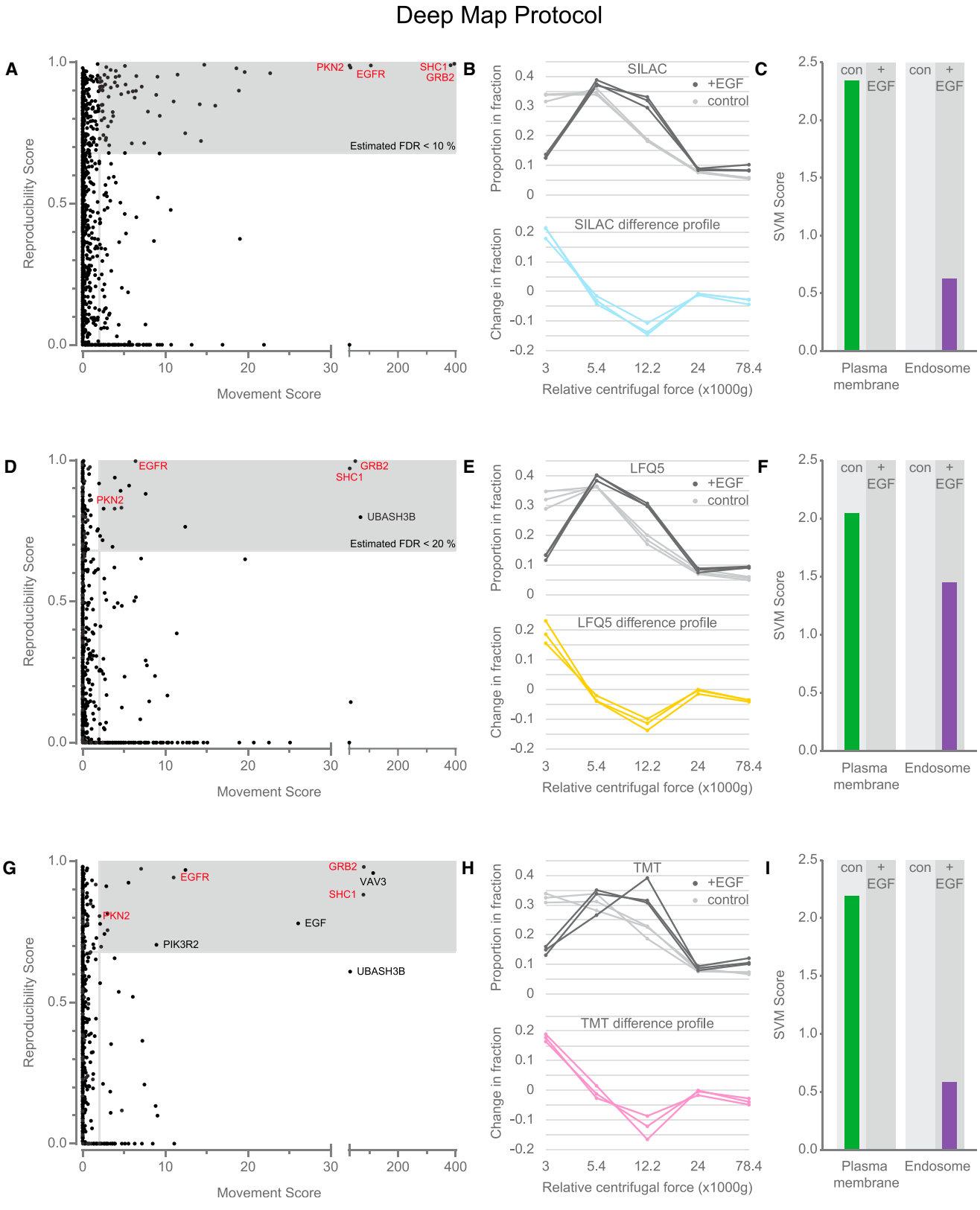

(legend on next page)

Table S2 for complete annotation). TMT and LFQ maps both detected sixteen movements but, in the case of LFQ, with a higher FDR. Of note, the improved depth of LFQ maps enabled the identification of UBASH3B movement, a protein absent from the SILAC dataset. Conversely, TMT was the only method to identify movement of EGF; this protein was not present in control cells and, hence, was excluded from LFQ and SILAC analyses, but, because of multiplexing of two maps, the TMT approach can handle such cases.

Key metrics and characteristics for static and dynamic applications of each method are summarized in Figure 4.

Application of LFQ Organellar Maps to Mouse Neurons

The successful implementation of LFQ organellar maps opened the possibility to investigate the spatial proteome of primary cells. To test this, we prepared acutely isolated neurons from embryonic mice (sacrificed at embryonic day 15 [E15]). At this stage of development, neurons show relatively little neurite arborization, which facilitates their isolation (Sciarretta and Minichiello, 2010). In total, five independent replicates were prepared on three separate days. Cells were lysed mechanically and subjected to our standard differential centrifugation scheme (Figure 5A). In addition to the six membrane fractions (LFQ6), we also collected the cytosol; this allowed us to capture the complete spatial and quantitative proteome from a single workflow despite very limited amounts of starting material (only 1–2 mg of protein/preparation). Samples were analyzed with the fast MS protocol (17.5 hr/preparation). In total, over 9,000 proteins were identified (Table S3). The combined output from all five replicates was then jointly processed to generate organellar maps; 3,894 proteins were profiled across all replicates. These were annotated with the same set of organellar markers as for HeLa cells, without any further cell-specific optimization (834 markers matched across species). Application of SVM machine learning showed a high overall marker prediction accuracy of 92.7% (with full cross-validation; Figure 5B). For a more detailed performance evaluation, we calculated F1 scores for each compartment cluster (Figure 5C). 11 of 12 clusters showed high resolution, with the exception of the (rather minor) endoplasmic reticulum (ER)-high curvature cluster. Stratification of the prediction classes (Figure 5D) revealed a large proportion of high-confidence predictions. Collectively, these data show that the performance of the LFQ neuron maps is extremely similar to what we had previously observed in HeLa cells (Figure 2; Figure S1) and demonstrate that the LFQ protocol is suitable for application to primary neurons.

In addition to the organellar localization data, our analysis also provided information on the global distribution across the membrane, nuclear, and cytosolic fractions for over 6,000 proteins. These included 1,120 proteins classified as mostly nuclear, 1,471 as mostly cytosolic, and 528 as nuclear and cytosolic (Table S4). Finally, we derived absolute protein abundances (i.e., copy numbers and cellular concentrations) for over 9,000 proteins using the proteomic ruler approach (Wiśniewski et al., 2014; Figure S4). Together, these data provide a comprehensive account of the mouse cortical neuron spatial proteome (Table S4).

A Quantitative Comparison of Mouse Neuron and HeLa Organellar Organization

The combined knowledge of protein abundance and subcellular localization data allows the reconstruction of cellular anatomy, as we have shown previously for HeLa cells (Itzhak et al., 2016). We prepared an equivalent analysis for primary mouse neurons (Figure 6). We derived a quantitative total proteome (Table S4), the contribution of every organelle to the whole cell protein mass, and also determined the protein composition of individual organelles. The availability of two spatial proteomes, HeLa and mouse neurons, prepared with the same approach and comparable depth of analysis, offered a unique opportunity for a systematic comparison of two very different cell types at the organellar level. HeLa cells are fast-growing immortal cells derived from a cervical carcinoma and are maintained in culture, whereas the neurons were differentiated mouse primary cells freshly isolated from the brain and had never been exposed to culture conditions. We sought to determine to what extent these differences are reflected at the compositional level.

At the qualitative proteome level, 78% (6,700) of all proteins detected in the neurons were also expressed in HeLa cells (assuming that proteins with the same name have orthologous functions in both organisms; Figure 6A). Our proteomic ruler data estimated that HeLa cells were approximately six times larger than the neurons. Factoring in relative protein abundance (copy numbers weighted by protein molecular weight and scaled by cell size), the composition overlap by protein mass drops to around 61%, demonstrating that quantitative and qualitative differences in protein expression both contribute

Figure 3. Assessment of Dynamic Organellar Maps with Different Quantification Strategies Using the Deep MS Protocol

(A) Three replicate SILAC experiments of cells left untreated or stimulated with EGF for 20 min were analyzed in a dynamic organellar maps experiment. The resulting difference profiles were subjected to statistical analysis to identify moving proteins (see Experimental Procedures for details). The movement and reproducibility scores for each protein are shown in an MR scatterplot; significantly moving proteins have high scores in both dimensions. The shaded area contains proteins where the estimated false discovery rate (FDR) for translocation is < 10% based on a mock control experiment.

(B) Top: the proportion of EGFR in each fraction across the differential centrifugation gradient for three replicates in control cells (gray lines) or cells stimulated with EGF (black lines). Bottom: the difference in protein pelleting in the fractions in untreated compared with EGF-treated cells for three replicates.

(C) Proteins in the shaded area of (A) were removed from the marker set, and all remaining proteins were subjected to organelle classification using SVM-based machine learning. The prediction scores for the plasma membrane and endosome are shown before and after treatment with EGF, correctly capturing the change in localization of the EGF receptor.

(D–F) The same as (A)–(C), respectively, but for LFQ-based (deep) experiments. Note that the shaded area corresponds to a translocation FDR of < 20%.

(G–I) Also the same as (A)–(C), respectively, but using data from the TMT-based (deep) experiments. Note that the shaded area is not FDR-controlled but uses cutoffs determined for the SILAC and LFQ experiments.

See also Figures S2 and S3 and Table S2.

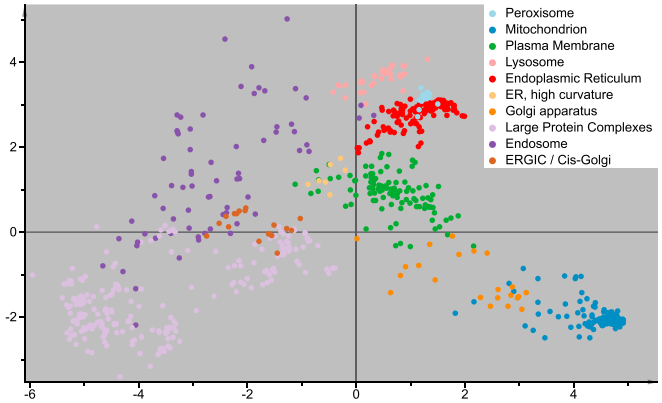

Fast	Deep	SILAC
37.5 h	112.5 h	Run time for 3 maps
2,100	3,700	Depth (proteins)
95.8 %	97.1 %	Prediction accuracy
0.91	0.94	Average F1 Score
+++	+++	Organellar Assignment
+++	+++	Dynamic Application
Best for cultured cells		

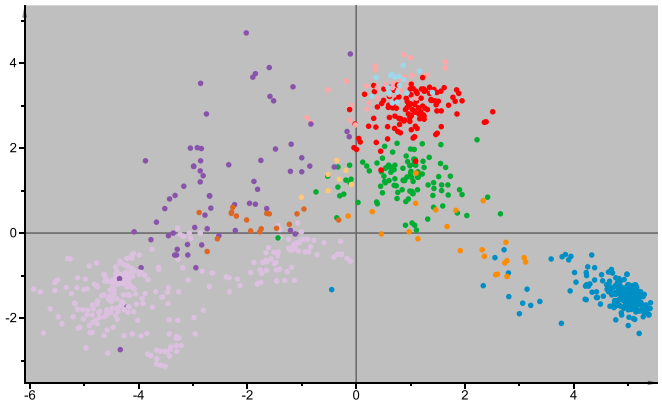

Fast	Deep	LFQ5
37.5 h	112.5 h	Run time for 3 maps
4,000	5,600	Depth (proteins)
89.5 %	90.8 %	Prediction accuracy
0.73	0.77	Average F1 Score
+	++	Organellar Assignment
+	+	Dynamic Application
Good for primary cells and tissues		

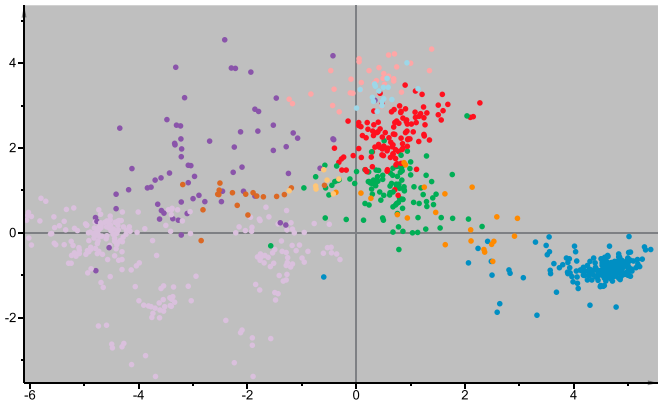

Fast	Deep	LFQ6
45 h	135 h	Run time for 3 maps
4,000	5,600	Depth (proteins)
92.4 %	94.7 %	Prediction accuracy
0.82	0.89	Average F1 Score
++	+++	Organellar Assignment
N/A	N/A	Dynamic Application
Good for primary cells and tissues		

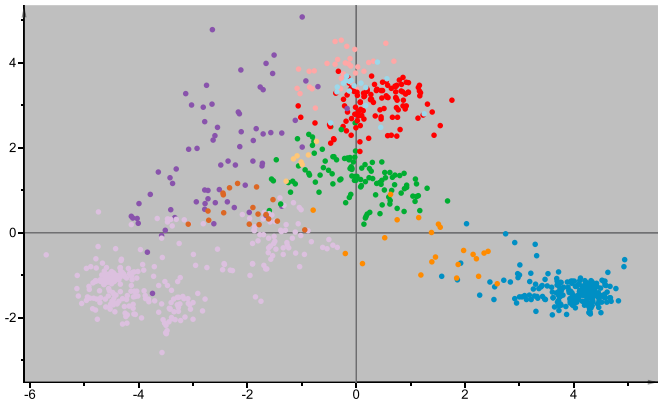

Fast	Deep	TMT
4.5 h	58.5 h	Run time for 3 maps
1,500	4,500	Depth (proteins)
91.3 %*	91.0 %	Prediction accuracy
0.74*	0.81	Average F1 Score
+/-	++	Organellar Assignment
++	++(+)	Dynamic Application
Best for high throughput		

(legend on next page)

substantially to cellular identity. Conversely, the perhaps surprisingly large degree of overlap suggests that, regardless of cell type, a considerable proportion of the proteome is relatively invariant. Similarly, in both cell types, the 100 most abundant proteins contribute over 30% of the total protein mass (Figure 6B).

We next compared the relative abundance of individual organelles (Figure 6C). In both cell types, mitochondria and the ER were the predominant organelles. For mitochondria, the contribution to total cell protein mass was almost double in HeLa cells (6.6% versus 3.4%), perhaps reflecting their increased need for energy to support continuous growth. In contrast, the ER contributed very similarly in both cells (3.7% in neurons and 4.4% in HeLa cells). The Golgi, endosomes, and lysosomes all made relatively minor overall contributions (all < 1%), although each of these organelles contributed ~2× greater mass to HeLa cells compared with neurons. The levels of ribosomes (approximately 5%–6%) and proteasomes (approximately 1%–1.5%) were remarkably similar (Figure 6D).

To facilitate the analysis of individual organelles, we identified the ten most abundant proteins in neuron organelles, which, in each case, make up a large proportion of the total organelle mass. We then compared the compositional overlap (by percent protein mass) with the corresponding HeLa cell organelles (Figures 6E–6I). As expected, the plasma membrane composition was radically different, both qualitatively and quantitatively, supporting the notion that the cell surface is a key factor in determining cellular identity (Sharma et al., 2015). Lysosomes also have very different compositions, but the differences are mostly quantitative; the neuronal lysosome is predominated by two cathepsins (Ctsb and Ctsd) that contribute 25% of the proteome, suggesting a specialized role for this compartment. In contrast, the ER has an almost identical composition in both cell types, suggesting that abundant ER constituents are indeed ''housekeeping'' proteins with similar concentrations across cell types. Of note, peroxisomes are also extremely similar in both cell types and dominated by the same protein, HSD17b4 (beta-hydroxysteroid dehydrogenase), which contributes 25% of the protein mass. Mitochondria show considerable compositional overlap but with specific metabolic adaptations (e.g., complete lack of CPS1 in neurons, a key component of the urea cycle and a major mitochondrial protein in HeLa cells; Itzhak et al., 2016). Although the levels of heat shock proteins are very similar in the ER (both approximately 20%), they are substantially lower in the mitochondria of neurons (approximately 9% versus 14% total); this may again relate to the high biosynthetic load imposed by rapidly growing HeLa cells. Thus, our analysis reveals qualitative and quantitative differences between neuronal and HeLa organelles but also a remarkable set of conserved features.

Outlook

Here we have established that SILAC, LFQ, and TMT are all highly effective for generating dynamic organellar maps through fractionation profiling, widely extending the scope of this method (summarized in Figure 4; Table S5). LFQ- and TMT-based profiling allow application to primary cells and tissues. As demonstrated for mouse neurons, the LFQ6 format is particularly useful is this regard because of its excellent prediction accuracy. We expect that a sixth fraction would also improve the prediction accuracy for TMT (using, for example, TMT 6-plex) but at the expense of the ability to place two maps in a single TMT 10-plex experiment. Conversely, using the protocols illustrated here, TMT maps required only ~50% (deep) or 12% (fast) of MS time compared with their SILAC or LFQ equivalents. Multiplexing is the biggest advantage of the TMT approach; with the fast protocol, a triplicate comparative analysis can be performed in as little as 9 hr of total MS measurement time, paving the way for high-throughput spatial proteomics experiments. For cells amenable to metabolic labeling, the SILAC approach offers exceptional performance both for organellar classification and for capture of translocation events. As reported previously (Itzhak et al., 2016) and as shown here, protein copy numbers estimated from the map data can be assigned to organellar proteomes to provide global cellular anatomy; all map formats are equally compatible with this approach.

EXPERIMENTAL PROCEDURES

Please refer to the Supplemental Experimental Procedures for complete details.

Analyzed Samples

For this study, we prepared multiple organellar maps from new samples but also re-analyzed several previously generated samples (Itzhak et al., 2016), either with new labeling and MS or new processing (see Supplemental Experimental Procedures for a complete description).

Cortical Neuron Preparation

Mice (C57BL/6 background) were housed in a specific pathogen-free (SPF) facility with a 12:12 hr light/dark cycle and food and water available ad libitum. All animal experiments were performed in compliance with institutional policies approved by the government of upper Bavaria. For preparation of cortical neurons from embryonic mice (E15), the procedure described in Meberg and Miller (2003) was adapted. This method yields fairly pure neuronal populations (Xu et al., 2012) because glial cells have not developed at this stage (Qian et al., 2000). Furthermore, these neurons have not yet formed extensive dendritic or axonal arbors and can therefore be isolated with relatively little cell damage (Sciarretta and Minichiello, 2010). In total, five independent preparations were analyzed by organellar mapping.

Figure 4. Visual Map Representation of 941 Marker Proteins Common to All Triplicate Deep Datasets (Left) and Key Metrics and Characteristics for Both Fast and Deep MS Protocols of the SILAC, LFQ5, LFQ6, and TMT Methods (Right)

Plots for the SILAC, LFQ5, and TMT methods were generated from a single principal-component analysis, where each marker protein had three different entries, one for each of the methods, and each entry had fifteen data points corresponding to three replicates of five fractions. Because LFQ6 has an additional data point for each map, an independent PCA was used to generate this plot; it was then scaled for optimum comparison with the other methods. All maps show highly similar separation and orientation of marker protein clusters, with increased cluster density of SILAC relative to other methods, most evident with the peroxisomal cluster. Furthermore, note that each plot is a 2D representation of a 15-dimensional dataset (18-dimensional for LFQ6); many seemingly overlapping clusters are resolved in higher dimensions not illustrated here. TMT fast maps include predictions for only 10 subcellular localizations; all other maps include 12.

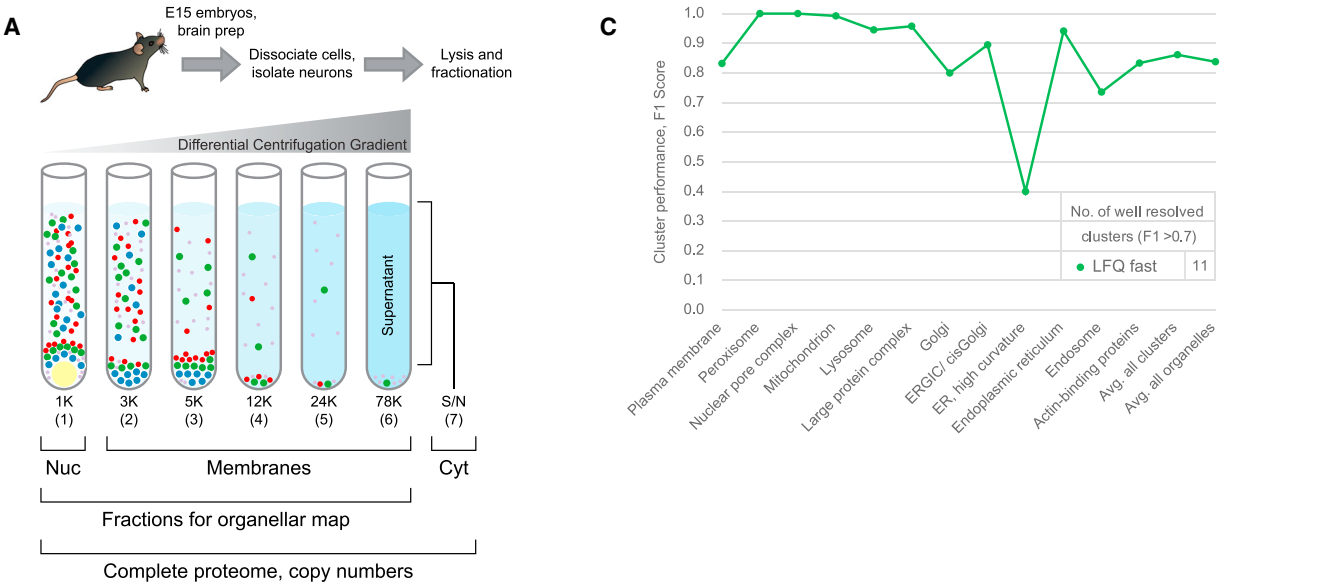

B

Summary statistics mouse neuron maps	
Analysis type	LFQ6, fast protocol
Replicates	5
MS time / map	17.5 hours
Proteins quantified	9,063
Mapped proteins (high + low res)	8,061
Mapped proteins (high res)	3,894
Average F1 score	0.86
High res prediction accuracy	92.7%

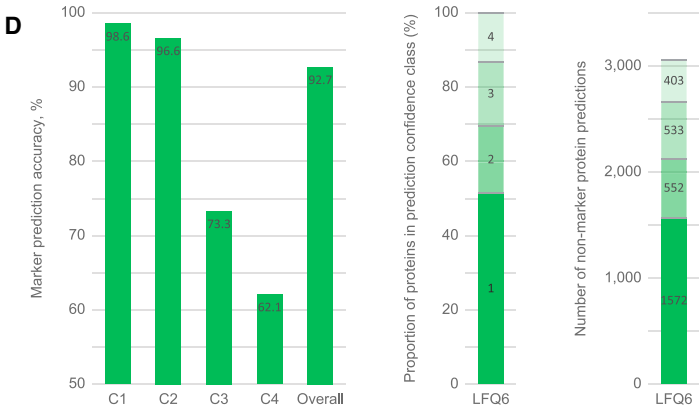

Figure 5. Application of Label-free Organellar Mapping to Mouse Neurons

(A) Schematic workflow. Cortical neurons were acutely isolated from embryonic mice, lysed mechanically, and subjected to a series of differential centrifugation steps: 1, nuclear-enriched fraction; 2–6, membrane fractions; 7, cytosol. All fractions were analyzed by label-free quantitative mass spectrometry. Fractions 1–6 were used to generate organellar maps. Fractions 1, 2–6 combined, and 7 were used to quantify proteins' nuclear, membrane-associated, and cytosolic pools. All fractions, 1–7 combined, were used to calculate protein copy numbers per cell.

(B) Summary of neuron map performance (combined output from five independent replicates).

(C) Detailed performance profiles of neuron maps. F1 scores were calculated as the harmonic mean of recall and precision, for each compartment, as in Figure 2G.

(D) Stratification of non-marker organellar predictions as in Figure 2H. The prediction accuracy of marker proteins within each class served as a proxy for the prediction accuracy of non-marker proteins. The first two classes had very high accuracies. Proportion and absolute number of non-marker predictions in each confidence class are shown in the center and on the right, respectively.

See also Figure S4 and Tables S3, S4, and S5.

Subcellular Fractionation Procedure for Label-free Organellar Maps

Cell lysis and subcellular fractionation were performed as reported previously (Itzhak et al., 2016) and as shown in Figure 1 but omitting any steps relating to the SILAC heavy-labeled reference sample. Each map was prepared from a single, ~70% confluent 15-cm dish of HeLa cells.

MS

Mass spectrometric analysis of LFQ and SILAC samples was performed with a Q Exactive HF (Thermo Fisher Scientific, Germany), as described previously (Itzhak et al., 2016). For samples in the TMT workflow, MS was performed with an Orbitrap Lumos or an Orbitrap Fusion instrument (Thermo Fisher Scientific, San Jose, CA).

Processing of MS Data

Raw files were processed with MaxQuant version 1.5 (Cox and Mann, 2008; Tyanova et al., 2016a) using the human or mouse reference protein datasets downloaded from UniProt (SwissProt canonical and isoforms database).

Statistical Methods

Generation of Organellar Maps

Each map experiment generated an abundance distribution profile across the subcellular fractions for every quantified protein; typically, several thousand proteins were profiled in an experiment. To allow cluster analysis, established marker proteins of various subcellular compartments were then identified from a previously defined set (Itzhak et al., 2016). For unsupervised clustering and

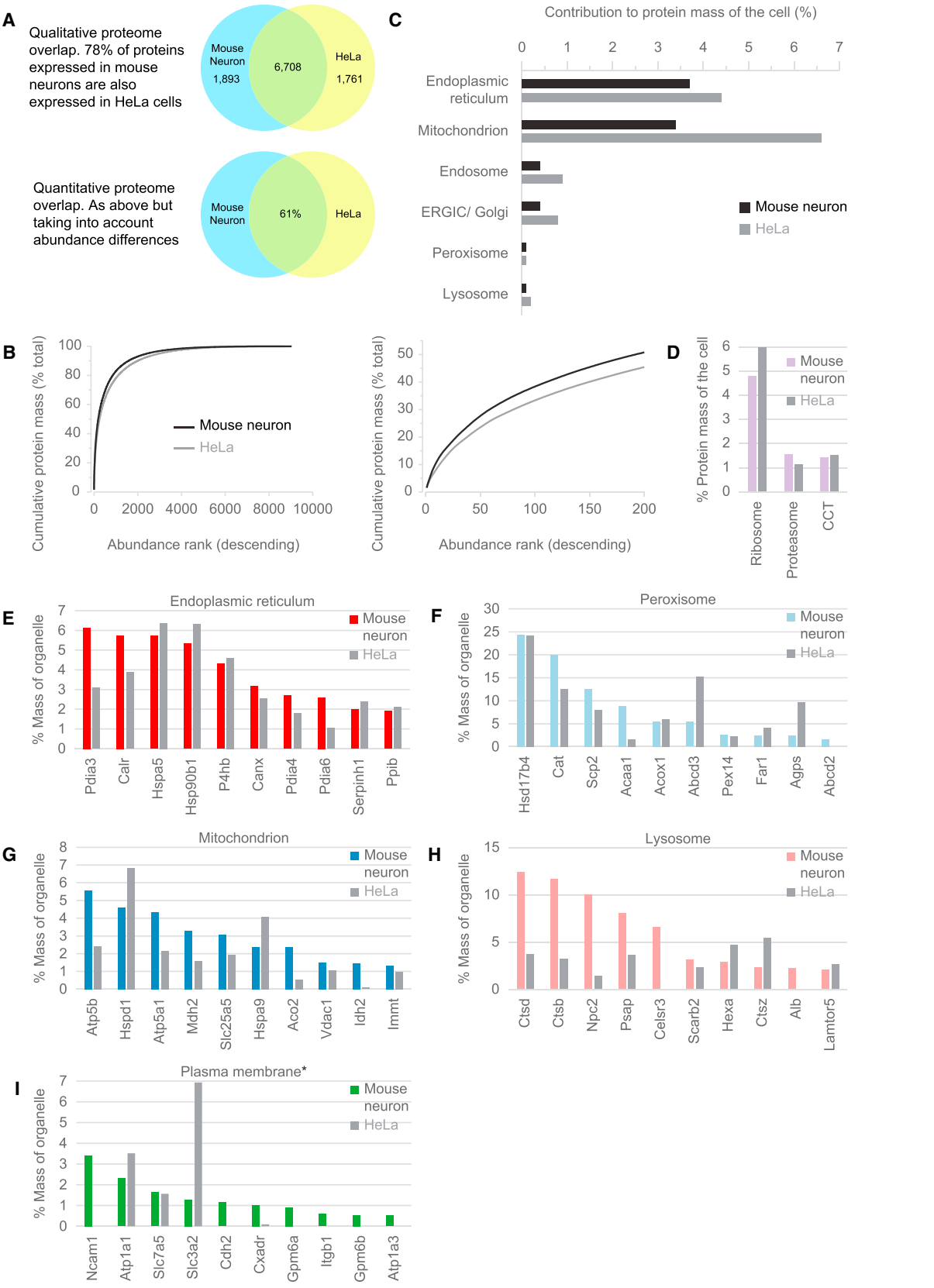

(legend on next page)

data visualization, profiles were subjected to principal-component analysis (PCA) (Figure 4). For unbiased and rigorous organellar assignments, the SVM-based supervised learning approach described in Itzhak et al. (2016), implemented in Perseus software (Tyanova et al., 2016b), was then applied. Conceptually, SVMs derive non-linear boundaries between multivariate data clusters. The SVMs were first trained with the marker protein profiles (using cross-validation to prevent overfitting). Non-marker proteins were then assigned to compartments based on the boundaries defined by the markers.

Detection of Dynamic Changes between Organellar Maps

The detection of protein translocations followed the procedure established in Itzhak et al. (2016), with several improvements and adaptations for the LFQ and TMT workflows (refer to the Supplemental Experimental Procedures for complete details). Briefly, the analysis is based on a two-tiered statistical test and fully FDR-controlled. First, for each protein, the two five-point profiles obtained from a pair of control and EGF treatment maps are subtracted to obtain a delta profile. All delta profiles are collected in a matrix, and for each delta profile, the robust Mahalanobis distance to the matrix center is calculated. The Mahalanobis distance approximately follows a chi-square distribution with five degrees of freedom and can therefore be converted into a p value (the likelihood to observe a profile as far or farther from the center). In total, three replicate pairs of control and EGF treatments were analyzed. For each protein, three p values for profile shifts were thus obtained. For a stringent analysis, the highest p value from the three replicates was chosen (corresponding to the smallest observed shift). This value was then cubed (because there were three independent replicates, each with a p value smaller or equal to the chosen one) and corrected for multiple hypothesis testing using the Benjamini-Hochberg method. The negative log10 of the corrected p value was the protein's M score ("magnitude" of movement). Large M scores correspond to large profile shifts. Second, the reproducibility of profile shifts was assessed. For each protein, the Pearson correlation between the delta profiles of replicates 1 versus 2, 1 versus 3, and 2 versus 3 was calculated. Of the three obtained R values, the lowest one was chosen and represents the R score ("reproducibility" of movement). Large R scores correspond to reproducible profile shifts. Genuinely translocating proteins have high M and R scores.

To achieve FDR control, data from a previous "mock" experiment (Itzhak et al., 2016) were used. Six control maps were split into three pairs and analyzed as described above. No genuine translocations were expected here. Applying the same M and R score cutoffs to the EGF treatment data and the mock data yielded the FDR, as the number of hits observed in the mock experiments divided by the number of hits in the EGF treatment experiments (scaled by the relative sizes of the datasets).

Software for Statistical Analysis and Graphics

Statistical analyses, data transformation, and filtering were performed in Perseus (Tyanova et al., 2016b), Prism 6 (GraphPad), and Microsoft Excel. Principal component analysis was performed in SIMCA 14 (Umetrics/MKS).

Copy-Number Determination and Organellar Composition Analysis

Copy numbers per cell, protein concentrations, and cell volumes were estimated with the proteomic ruler approach (Wiśniewski et al., 2014), implemented in Perseus software (Tyanova et al., 2016b). Organelle composition analysis was performed essentially as described in Itzhak et al. (2016).

Webpage

We have improved the web interface for our database of human subcellular localization predictions (http://www.MapOfTheCell.org).

SUPPLEMENTAL INFORMATION

Supplemental Information includes Supplemental Experimental Procedures, six figures, and five tables and can be found with this article online at http://dx.doi.org/10.1016/j.celrep.2017.08.063.

AUTHOR CONTRIBUTIONS

Conceptualization, D.N.I., C.D., M.P.W., and G.H.H.B.; Methodology, D.N.I., C.D., A.M., J.C., M.P.W., and G.H.H.B.; Formal Analysis, D.N.I. and G.H.H.B.; Investigation, D.N.I., C.D., R.A., and J.W.; Writing, D.N.I. and G.H.H.B.; Visualization, D.N.I. and G.H.H.B.; Website, S.T.; Supervision, M.P.W. and G.H.H.B.

ACKNOWLEDGMENTS

We thank Matthias Mann for his continued support of this project. This work was funded by the German Research Foundation (DFG/Gottfried Wilhelm Leibniz Prize MA 1764/2-1), the Louis-Jeantet Foundation, the Max Planck Society for the Advancement of Science, a Wellcome Trust Senior Clinical Research Fellowship 108070/Z/15/Z (to M.P.W.), and a strategic award to Cambridge Institute for Medical Research from the Wellcome Trust (100140). We are profoundly grateful to Korbinian Mayr, Igor Paron, and Gabriele Sowa for outstanding technical support. We give special thanks to Jan Rudolph for Perseus support and all members of the Mann Department for valuable feedback.

Received: April 26, 2017
Revised: July 14, 2017
Accepted: August 18, 2017
Published: September 12, 2017

REFERENCES

Aebersold, R., and Mann, M. (2016). Mass-spectrometric exploration of proteome structure and function. Nature *537*, 347–355.

Boisvert, F.M., Ahmad, Y., Gierlinski, M., Charriere, F., Lamont, D., Scott, M., Barton, G., and Lamond, A.I. (2012). A quantitative spatial proteomics analysis of proteome turnover in human cells. Mol. Cell. Proteomics *11*, M111.011429.

Christoforou, A., Mulvey, C.M., Breckels, L.M., Geladaki, A., Hurrell, T., Hayward, P.C., Naake, T., Gatto, L., Viner, R., Martinez Arias, A., and Lilley, K.S.

Figure 6. Comparative Organellar Anatomy of Mouse Neurons and HeLa Cells

(A) Full proteome overlap analysis. Top: qualitative overlap; the proportion of proteins detected in mouse neurons, with orthologs expressed in HeLa cells. Bottom: quantitative overlap (protein IDs and abundance considered).

(B) Proteins detected in neurons (black) or HeLa cells (gray) were ordered by abundance. The cumulative contribution to total cell protein mass was plotted on the y axis. In both cases, the 100 most abundant proteins contribute over one-third of the total protein mass (right).

(C) Relative contribution of individual organelles to total cell protein mass. Please note that the mouse neurons were acutely isolated; during this procedure, neurites, and, hence, parts of the plasma membrane, are lost (see Supplemental Experimental Procedures for details). This will lower the apparent plasma membrane contribution (which is not shown here for this reason) but is unlikely to substantially affect other organelles.

(D) Abundant protein complexes make remarkably similar contributions to the total proteome in both cell types. CCT, a multi-subunit chaperonin, is also known as TRiC.

(E–I) Compositional analysis of major organelles: (E) ER, (F) peroxisome, (G) mitochondrion, (H) lysosome, (I) plasma membrane. In each case, the ten most abundant proteins of the neuronal organelle were determined; the y axis shows their contributions to the total mass of the organelle. For comparison, the contributions of the same proteins to the corresponding HeLa organelles are shown (gray bars). Some organelles have extremely similar compositions (e.g., ER, peroxisome), others differ qualitatively (plasma membrane) or quantitatively (i.e., the same proteins but different distribution; e.g., lysosome). For the plasma membrane, only integral membrane proteins were considered. Although many synaptic marker proteins were detected in neuron lysates (Table S4), we did not observe a separate cluster corresponding to synapses.

(2016). A draft map of the mouse pluripotent stem cell spatial proteome. Nat. Commun. *7*, 8992.

Cox, J., and Mann, M. (2008). MaxQuant enables high peptide identification rates, individualized p.p.b.-range mass accuracies and proteome-wide protein quantification. Nat. Biotechnol. *26*, 1367–1372.

Cox, J., Hein, M.Y., Luber, C.A., Paron, I., Nagaraj, N., and Mann, M. (2014). Accurate proteome-wide label-free quantification by delayed normalization and maximal peptide ratio extraction, termed MaxLFQ. Mol. Cell. Proteomics *13*, 2513–2526.

Drissi, R., Dubois, M.L., and Boisvert, F.M. (2013). Proteomics methods for subcellular proteome analysis. FEBS J. *280*, 5626–5634.

Foster, L.J., de Hoog, C.L., Zhang, Y., Zhang, Y., Xie, X., Mootha, V.K., and Mann, M. (2006). A mammalian organelle map by protein correlation profiling. Cell *125*, 187–199.

Hesketh, G.G., Youn, J.Y., Samavarchi-Tehrani, P., Raught, B., and Gingras, A.C. (2017). Parallel Exploration of Interaction Space by BioID and Affinity Purification Coupled to Mass Spectrometry. Methods Mol. Biol. *1550*, 115–136.

Itzhak, D.N., Tyanova, S., Cox, J., and Borner, G.H. (2016). Global, quantitative and dynamic mapping of protein subcellular localization. eLife *5*.

Jadot, M., Boonen, M., Thirion, J., Wang, N., Xing, J., Zhao, C., Tannous, A., Qian, M., Zheng, H., Everett, J.K., et al. (2017). Accounting for Protein Subcellular Localization: A Compartmental Map of the Rat Liver Proteome. Mol. Cell. Proteomics *16*, 194–212.

Jean Beltran, P.M., Mathias, R.A., and Cristea, I.M. (2016). A portrait of the human organelle proteome in space and time during cytomegalovirus infection. Cell Syst. *3*, 361–373.e6.

Jean Beltran, P.M., Federspiel, J.D., Sheng, X., and Cristea, I.M. (2017). Proteomics and integrative omic approaches for understanding host-pathogen interactions and infectious diseases. Mol. Syst. Biol. *13*, 922.

Larance, M., and Lamond, A.I. (2015). Multidimensional proteomics for cell biology. Nat. Rev. Mol. Cell Biol. *16*, 269–280.

Mardakheh, F.K., Sailem, H.Z., Kümper, S., Tape, C.J., McCully, R.R., Paul, A., Anjomani-Virmouni, S., Jørgensen, C., Poulogiannis, G., Marshall, C.J., and Bakal, C. (2016). Proteomics profiling of interactome dynamics by colocalisation analysis (COLA). Mol. Biosyst. *13*, 92–105.

McAlister, G.C., Huttlin, E.L., Haas, W., Ting, L., Jedrychowski, M.P., Rogers, J.C., Kuhn, K., Pike, I., Grothe, R.A., Blethrow, J.D., and Gygi, S.P. (2012). Increasing the multiplexing capacity of TMTs using reporter ion isotopologues with isobaric masses. Anal. Chem. *84*, 7469–7478.

McAlister, G.C., Nusinow, D.P., Jedrychowski, M.P., Wühr, M., Huttlin, E.L., Erickson, B.K., Rad, R., Haas, W., and Gygi, S.P. (2014). MultiNotch MS3 enables accurate, sensitive, and multiplexed detection of differential expression across cancer cell line proteomes. Anal. Chem. *86*, 7150–7158.

Meberg, P.J., and Miller, M.W. (2003). Culturing hippocampal and cortical neurons. Methods Cell Biol. *71*, 111–127.

Ong, S.E., Blagoev, B., Kratchmarova, I., Kristensen, D.B., Steen, H., Pandey, A., and Mann, M. (2002). Stable isotope labeling by amino acids in cell culture, SILAC, as a simple and accurate approach to expression proteomics. Mol. Cell. Proteomics *1*, 376–386.

Qian, X., Shen, Q., Goderie, S.K., He, W., Capela, A., Davis, A.A., and Temple, S. (2000). Timing of CNS cell generation: a programmed sequence of neuron and glial cell production from isolated murine cortical stem cells. Neuron *28*, 69–80.

Rhee, H.W., Zou, P., Udeshi, N.D., Martell, J.D., Mootha, V.K., Carr, S.A., and Ting, A.Y. (2013). Proteomic mapping of mitochondria in living cells via spatially restricted enzymatic tagging. Science *339*, 1328–1331.

Sciarretta, C., and Minichiello, L. (2010). The preparation of primary cortical neuron cultures and a practical application using immunofluorescent cytochemistry. Methods Mol. Biol. *633*, 221–231.

Sharma, K., Schmitt, S., Bergner, C.G., Tyanova, S., Kannaiyan, N., Manrique-Hoyos, N., Kongi, K., Cantuti, L., Hanisch, U.K., Philips, M.A., et al. (2015). Cell type- and brain region-resolved mouse brain proteome. Nat. Neurosci. *18*, 1819–1831.

Tyanova, S., Temu, T., and Cox, J. (2016a). The MaxQuant computational platform for mass spectrometry-based shotgun proteomics. Nat. Protoc. *11*, 2301–2319.

Tyanova, S., Temu, T., Sinitcyn, P., Carlson, A., Hein, M.Y., Geiger, T., Mann, M., and Cox, J. (2016b). The Perseus computational platform for comprehensive analysis of (prote)omics data. Nat. Methods *13*, 731–740.

Weekes, M.P., Tomasec, P., Huttlin, E.L., Fielding, C.A., Nusinow, D., Stanton, R.J., Wang, E.C., Aicheler, R., Murrell, I., Wilkinson, G.W., et al. (2014). Quantitative temporal viromics: an approach to investigate host-pathogen interaction. Cell *157*, 1460–1472.

Wiśniewski, J.R., Hein, M.Y., Cox, J., and Mann, M. (2014). A "proteomic ruler" for protein copy number and concentration estimation without spike-in standards. Mol. Cell. Proteomics *13*, 3497–3506.

Xu, S.Y., Wu, Y.M., Ji, Z., Gao, X.Y., and Pan, S.Y. (2012). A modified technique for culturing primary fetal rat cortical neurons. J. Biomed. Biotechnol. *2012*, 803930.

Cell Reports, Volume *20*

Supplemental Information

A Mass Spectrometry-Based Approach for Mapping Protein Subcellular Localization Reveals the Spatial Proteome of Mouse Primary Neurons

Daniel N. Itzhak, Colin Davies, Stefka Tyanova, Archana Mishra, James Williamson, Robin Antrobus, Jürgen Cox, Michael P. Weekes, and Georg H.H. Borner


A
Fast, 1.5 h/map
Deep, 19.5 h/map
Fast, 12.5 h/map
Deep, 37.5 h/map
SILAC
TMT
Marker prediction Accuracy, %
No. of combined maps
B
LFQ6
LFQ5
TMT
SILAC
Concordance with SILAC Deep, %
Proportion of data, %
C
SILAC
LFQ5
LFQ6
TMT
Marker prediction accuracy, %
Class1
Class2
Class3
Class4
Overall
D
Proportion of proteins in prediction confidence class
SILAC
LFQ5
LFQ6
TMT
E
Number of non-marker protein predictions
SILAC
LFQ5
LFQ6
TMT
F
Cluster performance, F1 Score
No. of well resolved clusters (F1 >0.7)
SILAC deep 12
SILAC fast 12
Plasma membrane
Peroxisome
Nuclear pore complex
Mitochondrion
Lysosome
Large protein complex
Golgi
ERGIC/ cisGolgi
ER, high curvature
Endoplasmic reticulum
Endosome
Actin-binding proteins
Avg. all clusters
Avg. all organelles
G
Cluster performance, F1 Score
No. of well resolved clusters (F1 >0.7)
TMT deep 9
TMT fast 7
H
Cluster performance, F1 Score
No. of well resolved clusters (F1 >0.7)
LFQ5 deep 8
LFQ5 fast 7
I
Cluster performance, F1 Score
No. of well resolved clusters (F1 >0.7)
LFQ6 deep 12
LFQ6 fast 10

Figure S1. Further performance analyses of organellar maps generated with TMT, LFQ and SILAC quantification strategies. Related to Figure 2. A) Global prediction accuracy of maps made with TMT and SILAC workflows. Accuracy is the proportion of correctly predicted marker proteins; combining maps for classification increases prediction accuracy. *Please note that for TMT fast, classification was only performed on 10 clusters (see also G)). B) Concordance analysis for predictions made with the 'fast' MS protocol (three replicates combined). Predictions from the SILAC, TMT, and LFQ fast MS workflows were compared to the predictions obtained with the SILAC deep MS workflow, as in Figure 2K. C-E) Stratification of organellar predictions into confidence classes, as in Figure 2H-J, but for data obtained with the fast MS workflow. F-I): Detailed performance profiles of maps made with SILAC, LFQ5/6, and TMT, three replicates combined, comparing fast and deep MS protocols for each method. F1 scores are the harmonic mean of precision and recall of marker protein predictions for individual compartments. Clusters with F1 scores >0.7 have high predictive value.* For TMT fast maps, 'Nuclear pore complex' and 'ER high curvature' clusters had too few proteins to make SVM models, and were not included in the classification analysis; average F1 scores were hence calculated for only 10 clusters in this case. Peroxisomes were included, but not resolved (F1 = 0).

Fast Map Protocol

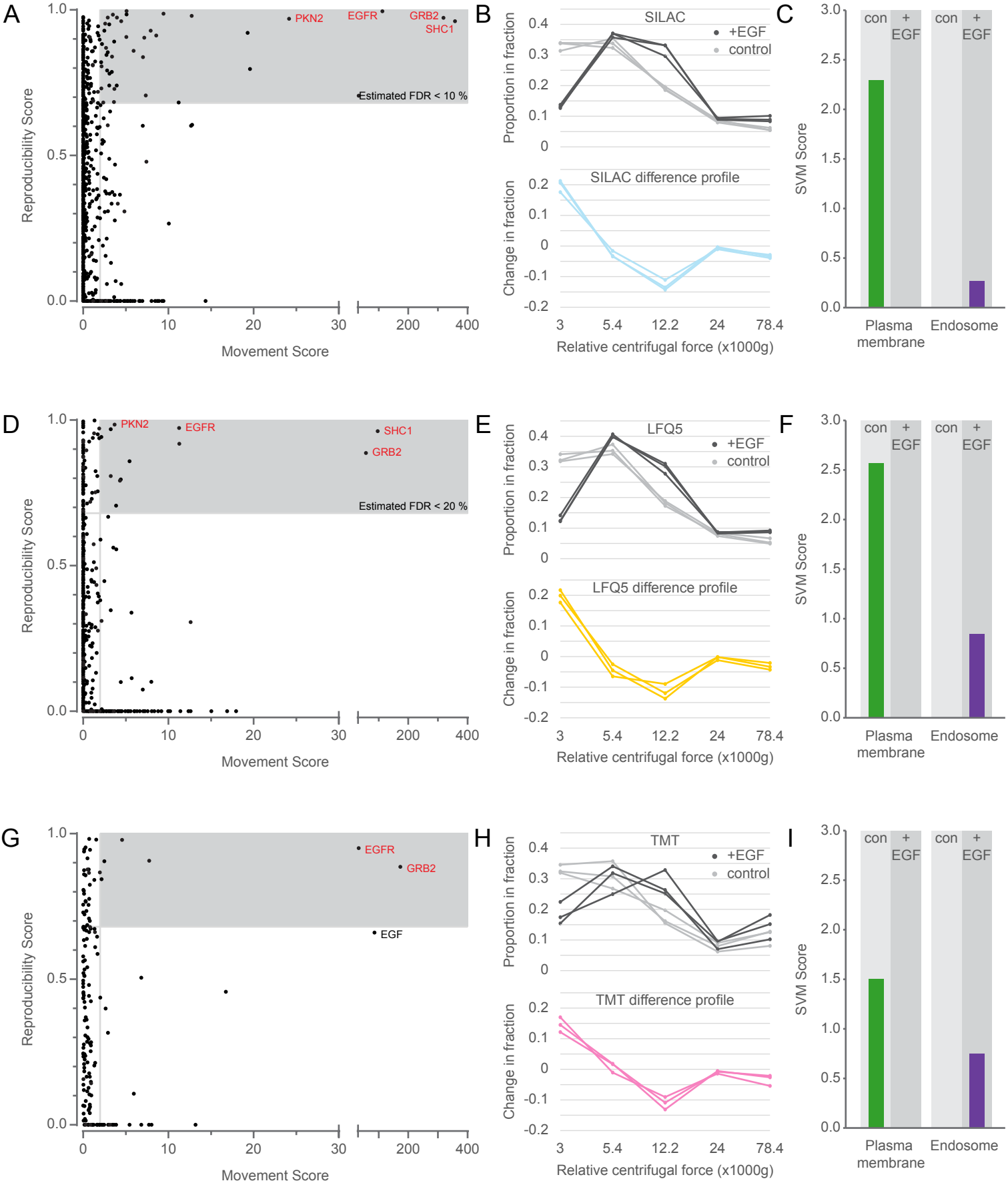

Figure S2. Assessment of Dynamic Organellar Maps with different quantification strategies using the fast MS protocol. Related to Figure 3. This figure is laid out exactly as Figure 3, except that data were generated with the fast MS protocol, which has reduced depth. Nonetheless, movement of EGFR from the plasma membrane to the endosome is captured with all methods.

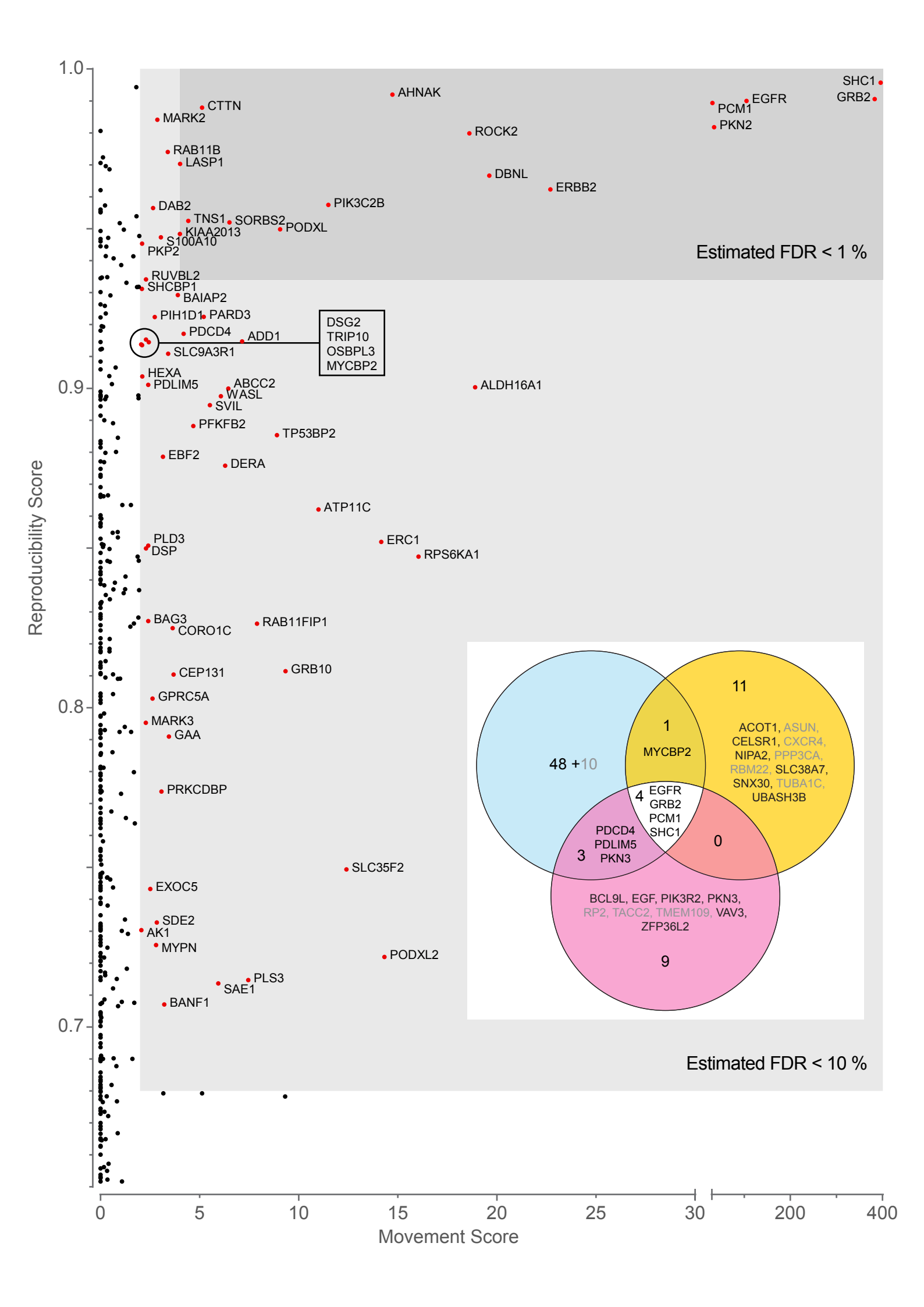
1.0
0.9
0.8
0.7
Reproducibility Score
0
5
10
15
20
25
30
200
400
Movement Score
SHC1
GRB2
EGFR
PCM1
PKN2
AHNAK
CTTN
MARK2
ROCK2
RAB11B
LASP1
DBNL
ERBB2
DAB2
PIK3C2B
TNS1
SORBS2
KIAA2013
PODXL
S100A10
PKP2
Estimated FDR < 1 %
RUVBL2
SHCBP1
BAIAP2
PIH1D1
PARD3
PDCD4
ADD1
SLC9A3R1
DSG2
TRIP10
OSBPL3
MYCBP2
HEXA
PDLIM5
ABCC2
WASL
SVIL
ALDH16A1
PFKFB2
TP53BP2
EBF2
DERA
ATP11C
PLD3
DSP
ERC1
RPS6KA1
BAG3
CORO1C
RAB11FIP1
CEP131
GRB10
GPRC5A
MARK3
GAA
PRKCDBP
SLC35F2
EXOC5
SDE2
AK1
MYPN
PODXL2
PLS3
SAE1
BANF1
48 +10
1
MYCBP2
11
ACOT1, ASUN, CELSR1, CXCR4, NIPA2, PPP3CA, RBM22, SLC38A7, SNX30, TUBA1C, UBASH3B
4
EGFR
GRB2
PCM1
SHC1
3
PDCD4
PDLIM5
PKN3
0
BCL9L, EGF, PIK3R2, PKN3, RP2, TACC2, TMEM109, VAV3, ZFP36L2
9
Estimated FDR < 10 %

Figure S3. Detailed view of EGF translocation analysis. Related to Figure 3. MR plot reproduced from Figure 3A with all 66 proteins identified as moving in response to EGF, based on the SILAC deep analysis, annotated with their gene names. Two shaded areas indicate two estimated FDRs based on a mock-control experiment; in the darker shaded area, less than 1% false positives are expected, while in the lighter shaded area <10% of false positives are expected. Inset, Venn diagram showing the overlap of moving proteins detected with the three methods (deep protocol), corresponding to Figure 3A, D, G; SILAC, blue, LFQ, yellow, and TMT, pink. Proteins that were present in the SILAC dataset but were identified as hits only in the TMT or LFQ method are coloured grey. Conversely, proteins not present in the SILAC dataset but identified as hits only in TMT or LFQ are shown in black. Furthermore, there were 8 proteins among the SILAC hits that were not present in the TMT dataset, and a further 2 proteins absent from the LFQ dataset, denoted by +10, in grey.

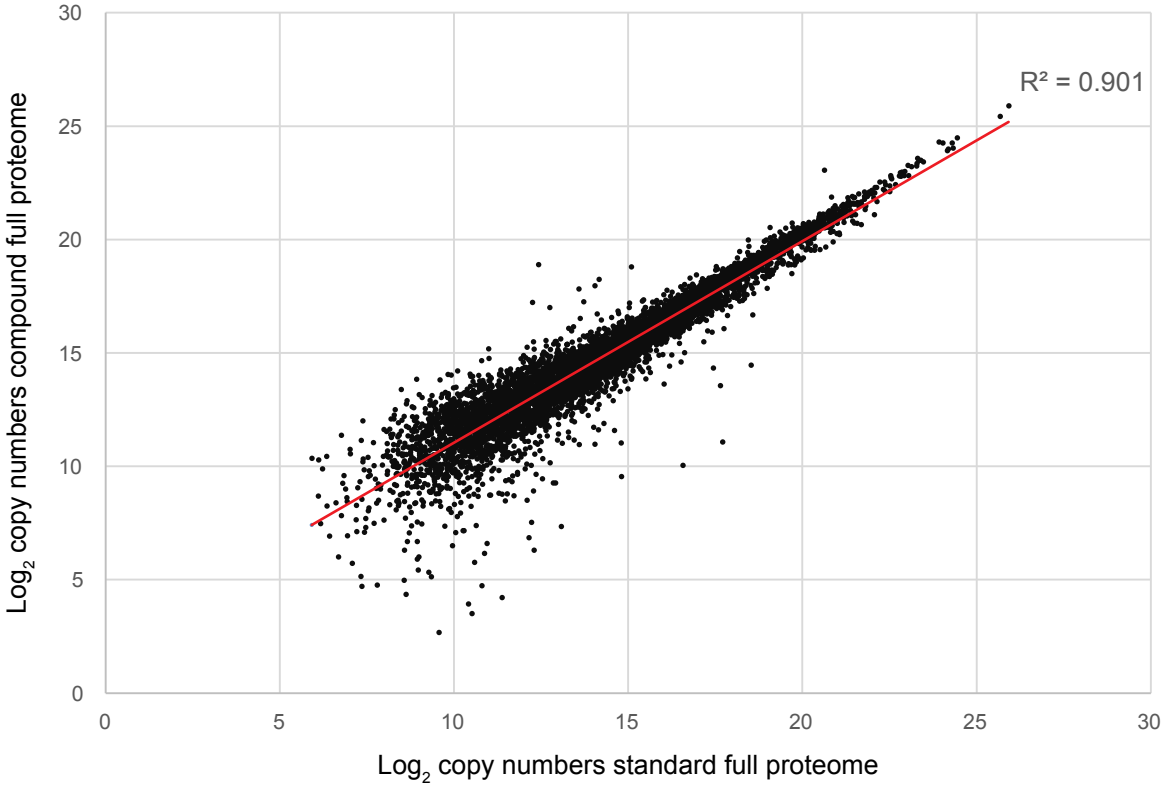
R² = 0.901
Log2 copy numbers compound full proteome
Log2 copy numbers standard full proteome
0
5
10
15
20
25
30

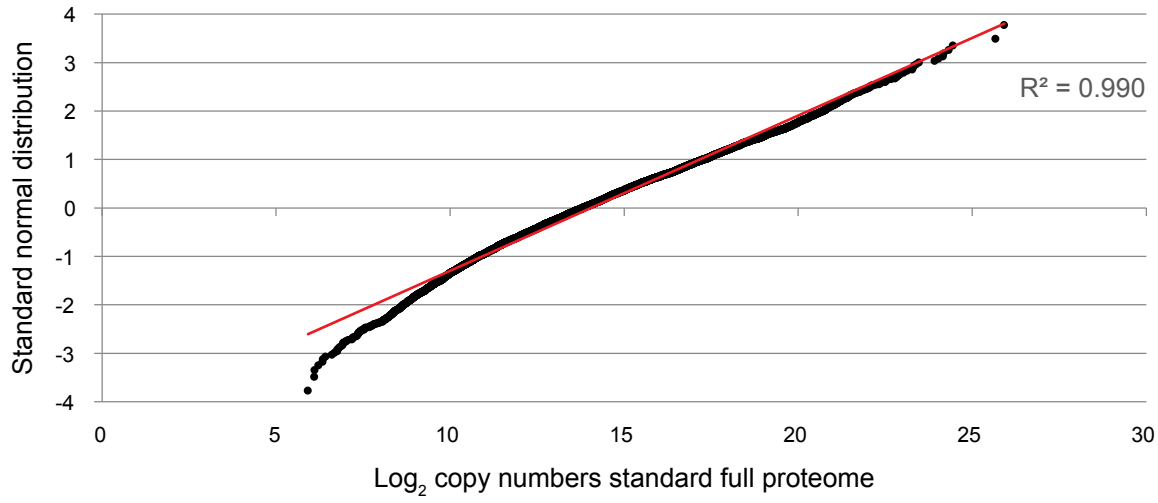
R² = 0.990
Standard normal distribution
Log2 copy numbers standard full proteome
4
3
2
1
0
-1
-2
-3
-4
0
5
10
15
20
25
30

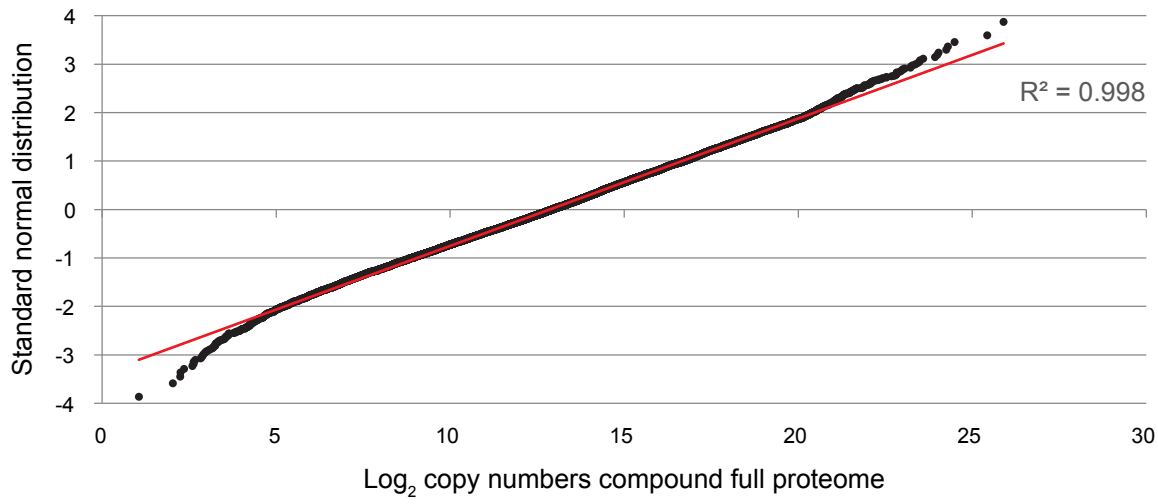
R² = 0.998
Standard normal distribution
Log2 copy numbers compound full proteome
4
3
2
1
0
-1
-2
-3
-4
0
5
10
15
20
25
30

Figure S4. Deriving protein copy numbers/cell with two different strategies. Related to Figure 5. Protein copy numbers per cell were calculated with the Proteomic Ruler approach (Wisniewski et al., 2014). This requires determination of a whole cell proteome by mass spectrometry as input. Here, two approaches were compared: the 'standard' full proteome measured from whole cell lysates, and a 'compound' full proteome obtained by combining the mass spectrometric measurements of seven subcellular fractions (Figure 5A, and Supplemental Experimental Procedures). This figure shows that both yield very consistent results, but the compound data has greater depth. A) Copy numbers of proteins common to both datasets show high levels of correlation ($R=0.949$, $R^2=0.9$), and very similar absolute values. B, C) Distribution of copy numbers obtained with the two methods. Data were log transformed, and analysed by QQ plots. Perfectly normally distributed data would follow a straight line. As can be seen, both datasets show excellent correlation with theoretical standard normally distributed data ($R^2>0.99$). Copy numbers from compound proteomes in C) have an extended dynamic range at the lower end.

Table S2, related to Figure 3: Literature search results on proteins that move significantly in response to stimulation with EGF, as annotated in Figure S3, related to Figure 3.

Canonical ID	Gene name	M SCORE	R SCORE	Supporting reference for involvement in EGF signalling
P29353	SHC1	395.9	0.996	(Sakaguchi et al., 1998)
Q09666	AHNAK	14.7	0.992	No previous link identified
P62993	GRB2	382.9	0.991	(Lowenstein et al., 1992)
P00533	EGFR	105.4	0.990	(Sherrill and Kyte, 1996)
Q15154	PCM1	31.3	0.989	(Akimov et al., 2011)
Q14247	CTTN	5.1	0.988	(Mader et al., 2011)
Q7KZI7	MARK2	2.9	0.984	No previous link identified
Q16513	PKN2	35.0	0.982	(Vincent and Settleman, 1997)*
O75116	ROCK2	18.6	0.980	(Julian and Olson, 2014)
Q15907	RAB11B	3.4	0.974	(Watanuki et al., 2014)
Q14847	LASP1	4.0	0.970	No previous link identified
Q9UJU6	DBNL	19.6	0.967	No previous link identified
P04626	ERBB2	22.7	0.962	(Karunagaran et al., 1996)
O00750	PIK3C2B	11.5	0.957	(Wheeler and Domin, 2001)
P98082	DAB2	2.7	0.956	(Eskova et al., 2014)
Q9HBL0	TNS1	4.4	0.952	(Pai et al., 2001)
O94875	SORBS2	6.5	0.952	(Soubeyran et al., 2003)
O00592	PODXL	9.1	0.950	(Larsson et al., 2016)
Q8IYS2	KIAA2013	4.0	0.948	No previous link identified
P60903	S100A10	3.0	0.947	No previous link identified
Q99959	PKP2	2.1	0.945	(Arimoto et al., 2014)
Q9Y230	RUVBL2	2.3	0.934	(Kozik et al., 2013)
Q8NEM2	SHCBP1	2.1	0.931	(Schmandt et al., 1999)
Q9UQB8	BAIAP2	3.9	0.929	(Lewis-Saravalli et al., 2013)
Q8TEW0	PARD3	5.2	0.922	(Wang et al., 2006)
Q9NWS0	PIH1D1	2.7	0.922	(Fan et al., 2009; Kamano et al., 2013)
Q53EL6	PDCD4	4.2	0.917	(Matsuhashi et al., 2014)
Q14126	DSG2	2.3	0.915	(Klessner et al., 2009)
P35611	ADD1	7.1	0.915	(Fukata et al., 1999)
Q15642	TRIP10	2.4	0.914	(Hu et al., 2009)
Q9H4L5	OSBPL3	2.1	0.914	No previous link identified
O75592	MYCBP2	2.1	0.914	(Holland et al., 2011)
O14745	SLC9A3R1	3.4	0.911	Uniprot*
P06865	HEXA	2.1	0.904	No previous link identified
Q96HC4	PDLIM5	2.4	0.901	Uniprot
Q8IZ83	ALDH16A1	18.9	0.900	No previous link identified
Q92887	ABCC2	6.4	0.900	No previous link identified
O00401	WASL	6.1	0.898	(Galovic et al., 2011)
O95425	SVIL	5.5	0.895	(Fang et al., 2010)
O60825	PFKFB2	4.7	0.888	(Novellasdemunt et al., 2013)
Q13625	TP53BP2	8.9	0.885	(Liu et al., 2015)
Q9HAK2	EBF2	3.2	0.879	No previous link identified
Q9Y315	DERA	6.3	0.876	No previous link identified
Q8NB49	ATP11C	11.0	0.862	Uniprot
Q8IUD2	ERC1	14.2	0.852	No previous link identified
Q8IV08	PLD3	2.4	0.851	(Tong et al., 2014)
P15924	DSP	2.3	0.850	(Lorch et al., 2004)
Q15418	RPS6KA1	16.1	0.847	(Zhang et al., 2015)
O95817	BAG3	2.4	0.827	No previous link identified
Q6WKZ4	RAB11FIP1	7.9	0.826	(Xu et al., 2016)

Q9ULV4	CORO1C	3.6	0.825	(Hosseinibarkooie et al., 2016)
Q13322	GRB10	9.3	0.811	(He et al., 1998)
Q9UPN4	CEP131	3.7	0.810	No previous link identified
Q8NFJ5	GPRC5A	2.6	0.803	(Zhong et al., 2015)
P27448	MARK3	2.3	0.795	No previous link identified
P10253	GAA	3.5	0.791	No previous link identified
Q969G5	PRKCDBP	3.1	0.774	Uniprot
Q8IXU6	SLC35F2	12.4	0.749	No previous link identified
O00471	EXOC5	2.5	0.743	(Fogelgren et al., 2014)
Q6IQ49	SDE2	2.8	0.733	No previous link identified
P00568	AK1	2.1	0.730	No previous link identified
Q86TC9	MYPN	2.8	0.726	No previous link identified
Q9NZ53	PODXL2	14.3	0.722	No previous link identified
P13797	PLS3	7.5	0.715	(Hosseinibarkooie et al., 2016)
Q9UBE0	SAE1	5.9	0.714	No previous link identified
O75531	BANF1	3.2	0.707	No previous link identified

A primary literature search was conducted to identify links between EGF receptor signalling and the identified hits; references for these links are provided where possible. This search was not exhaustive; some links may have been missed, and apologies are made to those whose work was not cited. *a link between this protein and EGFR was not identified, but a link between this and a second hit in the list, which is linked to EGFR signalling, was identified.

Table S5, related to Figure 5: Comparison of spatial proteomic profiling methods

Method	**Dynamic Organellar Maps**		**hyperLOPIT**	**PCP**	**Rat liver proteome**
Reference	Itzhak et al., 2016	This Study	Christoforou et al., 2016	Foster et al., 2006	Jadot et al., 2017
Organelle separation technique	Differential centrifugation		Density gradient centrifugation	Velocity gradient centrifugation	Combination of different centrifugation techniques
Quantification approach	Metabolic labelling (SILAC)	Label free quantification (LFQ) or Isobaric labelling (TMT)	Isobaric labelling	Label free quantification	Isobaric labelling
Instrumentation	Q Exactive HF	Q Exactive HF (for LFQ) Orbitrap Fusion/Lumos (for TMT)	Orbitrap Fusion	Orbitrap*	Orbitrap Velos
Starting material per map	1E7 HeLa cells	1 -2 mg protein (mouse neurons, for LFQ)	1E8 mouse embryonic stem cells	1 mouse liver	2 rat livers
Number of MS analysis runs per map	24	7 (LFQ)	24	32	>200
Number of mapped proteins	>8,700 (from 6 replicates)	>8,000 (from 5 replicates)	>5,500 (from 2 replicates)	>1,400*	>6,000 (from 4 replicates)
Strengths of the method	High organellar resolution High reproducibility allows comparative applications Quantitative organellar modelling		High organellar resolution Comparative applications (Jean Beltran et al., 2016)	Assignment of one protein to multiple organellar compartments possible	Assignment of one protein to multiple organellar compartments, with quantification

*The performance of mass spectrometers has substantially improved since the publication of PCP in 2006; a repeat analysis with current MS instruments would very likely show a depth of analysis comparable to the other methods.

Supplemental Experimental Procedures

Analysed samples - Overview

In this study, we prepared maps from several new samples, but also re-analysed several previously generated samples (Itzhak et al., 2016), either with new labelling and new mass spectrometry (MS), or new processing (summarised in the table below). All analyses were performed with fast (short MS run time) and deep (extensive MS run time) protocols.

The aim of the study was two-fold: firstly, to develop and evaluate workflows for Label-Free Quantification (LFQ) and Tandem Mass Tagging (TMT)-based organellar maps; and secondly, to compare the performance of different labelling strategies for comparative Dynamic Organellar Maps. To establish the label-free workflow, six maps were prepared from fresh samples (HeLa untreated). To ensure a fair comparison of SILAC, TMT, and LFQ approaches for dynamic applications, maps were prepared from the exact same set of samples, generated previously (HeLa untreated vs HeLa stimulated with EGF (Itzhak et al., 2016)). This published set was SILAC labelled, and analysed in a 'fast' format (Itzhak et al., 2016). Here, a 'deep' analysis of the same samples was added (i.e. a new in-depth MS analysis). For TMT maps, SILAC light subfractions were labelled with TMT reagent, and analysed by MS. For dynamic LFQ maps, SILAC RAW files were re-processed in MaxQuant software, ignoring the heavy channel, to simulate a label-free experiment (see 'Processing of mass spectrometry data' below for details).

Samples analysed in this study

Sample ID	Sample, treatment (Reference), original labelling	Labelling for this study	Mass spec method	Reprocessed or New Mass spec analysis	Used for
1	3 x HeLa, untreated (Itzhak et al., 2016), SILAC light subfractions and heavy reference fraction	SILAC	Deep	Reprocessed	SILAC maps, static
2	3 x HeLa, untreated (Itzhak et al., 2016), SILAC light subfractions and heavy reference fraction	SILAC	Fast	Reprocessed	SILAC maps, static
		SILAC	Fast	Reprocessed	SILAC maps, dynamic
		SILAC	Deep	New mass spec	SILAC maps, dynamic
3	3 x HeLa, 20 min EGF treated (Itzhak et al., 2016), SILAC light subfractions and heavy reference fraction	SILAC	Fast	Reprocessed	SILAC maps, dynamic
		SILAC	Deep	New mass spec	SILAC maps, dynamic
1	6 x HeLa, untreated (Itzhak et al., 2016), SILAC light subfractions and heavy reference fraction	SILAC	Deep	Reprocessed	SILAC maps, 'mock' dynamic (for FDR control)
4	6 x HeLa, untreated (this study), no label (3 of them selected for additional deep analysis)	Label free	Fast	New mass spec	LFQ maps, static
		Label free	Deep	New mass spec	LFQ maps, static
2	3 x HeLa, untreated (Itzhak et al., 2016), SILAC light subfractions and heavy reference fraction	Process as label free	Fast	Reprocessed	LFQ maps, dynamic
		Process as label free	Deep	New mass spec	LFQ maps, dynamic
3	3 x HeLa, 20 min EGF treated (Itzhak et al., 2016), SILAC light subfractions and heavy reference fraction	Process as label free	Fast	Reprocessed	LFQ maps, dynamic
		Process as label free	Deep	New mass spec	LFQ maps, dynamic
1	6 x HeLa, untreated (Itzhak et al., 2016), SILAC light subfractions and heavy reference fraction	Process as label free	Deep	Reprocessed	LFQ maps, 'mock' dynamic (for FDR control)

2	3 x HeLa, untreated (Itzhak et al., 2016), SILAC light subfractions only	TMT 10-plex	Fast	New mass spec	TMT maps, static and dynamic
		TMT 10-plex	Deep	New mass spec	TMT maps, static and dynamic
3	3 x HeLa, 20 min EGF treated (Itzhak et al., 2016), SILAC light subfractions only	TMT 10-plex	Fast	New mass spec	TMT maps, dynamic
		TMT 10-plex	Deep	New mass spec	TMT maps, dynamic
5	5 x mouse neurons, acutely isolated, no label (this study)	Label free	Fast	New mass spec	LFQ maps of mouse neurons

Cell Culture

For the generation of label-free organellar maps, HeLa cell cultures were maintained as described (Itzhak et al., 2016), but using regular Dulbecco's Modified Eagle's Medium (DMEM) and fetal calf serum (instead of SILAC labelling medium and dialysed fetal calf serum).

Subcellular fractionation procedure for label-free organellar maps

Cell lysis and subcellular fractionation were identical to our previously reported protocol (Itzhak et al., 2016), but omitting any steps relating to the SILAC heavy labelled reference sample. Each map was prepared from a single ~70% confluent 15 cm dish of HeLa cells.

Cortical neuron preparation

Mice (C57BL/6 background) were housed in an SPF facility with 12:12 h light/dark cycle and food/water available ad libitum. All animal experiments were performed in compliance with institutional policies approved by the government of upper Bavaria. For preparation of cortical neurons, the procedure described in Meberg and Miller (2003) was adapted. One E15 pregnant mice was sacrificed by cervical dislocation, the uterus was removed from the abdominal cavity and placed into a 10 cm sterile petri dish containing cold Hanks' balanced salt solution (HBSS) on ice. Each fetus was isolated, heads of embryos were quickly cut, brains were removed from the skull and immersed in ice cold HBSS. Subsequently, cortical hemispheres were dissected and meninges were removed under a stereo-microscope. For each sample, cortical tissue from typically six to seven embryos (from one litter) was cut into smaller pieces, transferred to 15 ml sterile tube and treated with 0.25% trypsin containing 1 mM EDTA for 20 minutes at 37°C. The enzymatic reaction was stopped by removing the supernatant and washing the tissue twice with Neurobasal medium (Invitrogen) containing 5% Fetal Bovine Serum. The tissue was resuspended in 2 ml medium and triturated 10 strokes with the tip of a Pasteur pipette. Single cell suspension was achieved by triturating an additional 10 strokes with a fire-polished pipette. Cells were spun at 180 x g, the supernatant was removed and the cell pellet was stored on ice till further use.

Please note that this preparation procedure yields fairly pure neuronal populations (Xu et al., 2012), since glial cells have not yet developed at stage E15 (Qian et al., 2000). Supporting this notion, we detected neuronal markers as highly abundant proteins in our complete neuron proteome (Table S4; eg Nestin, 91th abundance percentile; Tubb3, 98th abundance percentile), whereas markers of glial cells (eg GFAP (astrocyte marker) and Cldn11/Ops (oligodendrocyte marker)) were undetectable. Red blood cells were a very minor contaminant of the preparation (estimated at ca. 1.5%, based on levels of detected hemoglobin). Since the red blood cell proteome is mostly dominated by hemoglobin itself (Bryk and Wisniekswi, 2017), the contamination of the neuron proteome with other red blood cell proteins was considered negligible.

Owing to the necessary cell dissociation step, isolated neurons are prone to losing their neurites during the preparation procedure. Since cells can be cultured subsequently (Meberg and Miller, 2003), this does not appear to compromise cell viability. The axonal and dendritic parts of the plasma membrane (in addition to a proportion of cytosol) are hence lost to some extent, and will not be accounted for in the proteome. This is unavoidable for the analysis of acutely isolated neurons. Importantly, at this early stage of development, there is not extensive dendritic or axonal arborisation (Sciarretta and Minichiello, 2010), so the loss of neurites should account for a fairly small proportion of the total cellular material. The big advantage of using acutely isolated neurons is that

the cells have not been exposed to any culture conditions, and, with the above restrictions, should faithfully reflect neuronal composition as encountered in the brain.

Generation of organellar maps from neurons

In total, six independent neuron preparations were performed, on three separate days (two pregnant females/day). Isolated neurons were immediately processed for organellar mapping. For generation of Map 1, neurons from preparations 1&2 were pooled. For Maps 2-5, neurons prepared from a single litter were used. A typical prep corresponded to 1-2 mg of protein as starting material for subcellular fractionation.

Cells were resuspended in ice-cold PBS and centrifuged at 250 x g for 5 minutes. Cells were then resuspended in 5 ml homogenisation buffer (25 mM Tris pH 7.4, 50 mM Sucrose, 0.2 mM EGTA, 0.5 mM MgCl2) for 5 minutes. For Map 1, cells were lysed in a Dounce homogenizer (Sartorius, tight pestle; 15 strokes). For Maps 2-5, cells were passed through a cell cracker (Isobiotec) fitted with a 10 µm bore (5 passes) to achieve lysis. The remainder of the fractionation protocol followed the procedure previously described in detail for HeLa cells (Itzhak et al., 2016).

Sample preparation for mass spectrometry

SILAC and LFQ samples

Protein digestion, peptide cleanup and peptide fractionation of label free and SILAC based samples were performed as described (Itzhak et al., 2016).

TMT sample preparation

Protein fractions in SDS buffer (2.5% SDS, 50 mM Tris pH 8.1) were precipitated with 100% acetone and resuspended in 6M guanidine, 50 mM HEPES pH 8.5. Dithiothreitol (DTT) was added to a final concentration of 5 mM and samples were incubated for 20 minutes. Cysteines were alkylated with 14 mM iodoacetamide and incubated 20 minutes at room temperature in the dark. Excess iodoacetamide was quenched with DTT for 15 min. Samples were diluted with 200 mM HEPES pH 8.5 to 1.5 M Guanidine, followed by digestion at room temperature for 3 hr with LysC protease at a 1:100 protease-to-protein ratio. Following LysC digestion, trypsin was then added at a 1:100 protease-to-protein ratio followed by overnight incubation at 37°C. The reaction was quenched with 2% formic acid, subjected to C18 solid-phase extraction (Sep-Pak, Waters) and vacuum-centrifuged to near-dryness. TMT labelling was performed as previously described (Weekes et al., 2014). Briefly, desalted peptides were dissolved in 200 mM HEPES pH 8.5. Peptide concentration was measured by micro BCA (Pierce), and 25 µg of peptide labelled with TMT reagent at a final (AcN) concentration of 30% (v/v). Samples were labelled as follows: Control 3k (TMT 126); Control 5.4k (TMT 127N); Control 12.2k (TMT 127C); Control 24k (TMT 128N); Control 78.4k (TMT 128C); EGF-treated 3k (TMT 129N); EGF-treated 5.4k (TMT 129C); EGF-treated 12.2k (TMT 130N); EGF-treated 24k (TMT 130C); EGF-treated 78.4k (TMT 131). Following incubation at room temperature for 1 h, the reaction was quenched with hydroxylamine to a final concentration of 0.5% (v/v). TMT-labeled samples were combined at a 1:1:1:1:1:1:1:1:1:1 ratio. The sample was vacuum-centrifuged to near dryness and subjected to C18 solid-phase extraction (SPE) (Sep-Pak, Waters).

Off-line high pH reversed-phase (HpRP) peptide fractionation of TMT labelled samples (deep protocol)

TMT-labelled tryptic peptides were subjected to HpRP-HPLC fractionation using an Ultimate 3000 RSLC UHPLC system (Thermo Fisher Scientific) equipped with a 2.1 i.d x25 cm, 1.7 µm particle Kinetix Evo C18 column (Phenomenex). Mobile phase consisted of A: 3% AcN, B: AcN and C: 200 mM ammonium formate pH 10. Isocratic conditions were 90% A/10% C and C was maintained at 10% throughout the gradient elution. Separations were carried out at 45°C. After loading at 200 µL/minute for 5 minutes and ramping the flow rate to 400 µL/minute over 5 minutes the gradient elution proceed as follows: 0-19% B over 10 minutes (curve 3), 19-34% B over 14.25 minutes (curve 5), 34-50% B over 8.75 minutes (curve 5), followed by a 10 minutes wash at 90% B. UV absorbance was monitored at 280 nm and 15 s fractions were collected into 96 well microplates using the integrated fraction collector. Peptide containing fractions were then orthogonally recombined into 24

fractions and dried in a vacuum centrifuge and resuspended in 10 µL MS solvent (4% AcN / 5% formic acid (FA) prior to LC-MS3). 12 combined fractions were used for MS analysis of replicates 1 and 3. In replicate 2, a contaminant of unknown origin reduced the MS performance; hence, all 24 combined fractions were used for MS analysis.

Mass spectrometric (MS) analysis

SILAC and LFQ samples

Mass spectrometric analysis of SILAC and LFQ samples was performed as described (Itzhak et al., 2016). Briefly, peptides were loaded onto a 50-cm column with 75-µm inner diameter, packed in-house with 1.8-µm C18 particles (Dr Maisch GmbH, Germany), attached to an EASY-nLC 1000 (Thermo Fisher Scientific, Germany). Peptide separation was achieved with a binary buffer system consisting of 0.1% formic acid (buffer A), and 80% acetonitrile in 0.1% formic acid (buffer B), using a linear gradient of buffer B from 2% to 30% in 130 min followed by washout (ramping to 95% B in 5 min, constant at 95% B for 5 min, ramping down to 2% B in 5 min, constant at 2% B for 5 min), at a flow rate of 250 nl/min. The column was operated at 55°C. The LC was coupled to a Q Exactive HF Hybrid Quadrupole-Orbitrap mass spectrometer (Thermo Fisher Scientific, Germany). MS data were acquired using a data-dependent top 15 method. Survey scans were acquired at a resolution of 120,000, and HCD spectra at a resolution of 15,000. The dynamic exclusion of sequenced peptides was set to 30s.

TMT samples

For samples in the TMT workflow, mass spectrometry data for replicates 1 and 2 was acquired with an Orbitrap Lumos and replicate 3 with an Orbitrap Fusion (Thermo Fisher Scientific, San Jose, CA).

Mass spectrometric analysis of TMT samples with an Orbitrap Lumos

Samples were injected onto an Ultimate 3000 RSLC nano UHPLC equipped with a 300 µm i.d. x 5 mm Acclaim PepMap µ-Precolumn (Thermo Fisher Scientific) and a 75 µm i.d. x50 cm 2.1 µm particle Acclaim PepMap RSLC analytical column. Loading solvent was 0.1% FA, analytical solvent A: 0.1% FA and B: AcN + 0.1% FA. All separations are carried out at 55°C. Samples were loaded at 5 µL/minute for 5 minutes in loading solvent before beginning the analytical gradient. The following gradient was used: 3-7% B over 4 minutes, 7 – 37% B over 176 minutes, followed by a 10 minutes wash at 90% B and equilibration at 3% B for 5 minutes. Each analysis on the Orbitrap Lumos mass spectrometer (Thermo Fisher Scientific) used a MultiNotch MS3-based TMT method (McAlister et al., 2012, 2014). The following settings were used: MS1: 400-1200 Th, Quadrupole isolation, 120,000 Resolution, $2x10^5$ AGC target, 50 ms maximum injection time, ions injected for all parallisable time. MS2: Quadrupole isolation at an isolation width of m/z 0.7, CID fragmentation (NCE 35) with ion trap scanning out in turbo mode from m/z 120, $1.5x10^4$ AGC target, 120 ms maximum injection time, ions accumulated for all parallisable time in centroid mode. MS3: In Synchronous Precursor Selection mode the top 10 MS2 ions were selected for HCD fragmentation (NCE 65) and scanned out in the Orbitrap at 60,000 resolution with an AGC target of $1x10^5$ and a maximum accumulation time of 150 ms, ions were not accumulated for all parallelisable time. The entire MS/MS/MS cycle had a target time of 3 s. Dynamic exclusion was set to +/- 10 ppm for 70 s. MS2 fragmentation was trigged on precursors $5x10^3$ counts and above.

Mass spectrometric analysis of TMT samples with an Orbitrap Fusion

Samples were injected onto an Ultimate 3000 RSLC nano UHPLC equipped with a 300 µm i.d. x 5 mm Acclaim PepMap µ-Precolumn (Thermo Fisher Scientific) and a 75 µm i.d. x50 cm 2.1 µm particle Acclaim PepMap RSLC analytical column. Loading solvent was 0.1% TFA, analytical solvent A: 0.1% FA and B: AcN + 0.1% FA. All separations are carried out at 55°C. Samples were loaded at 10 µL/minute for 5 minutes in loading solvent before beginning the analytical gradient. The following gradient was used: 3-5.6% B over 4 minutes, 5.6 – 32% B over 162 minutes, followed by a 5 minute wash at 80% B and a 5 minute wash at 90% B and equilibration at 3% B for 5 minutes. Each analysis on the Orbitrap Lumos mass spectrometer (Thermo Fisher Scientific) used a MultiNotch MS3-based TMT method (McAlister et al., 2012, 2014). The following settings were used: MS1: 400-1400 Th, Quadrupole isolation, 120,000 Resolution, $2x10^5$ AGC target, 50 ms maximum injection time, ions injected for all parallisable time. MS2: Quadrupole isolation at an isolation width

of m/z 0.7, CID fragmentation (NCE 30) with ion trap scanning out in rapid mode from m/z 120, $1x10^4$ AGC target, 70 ms maximum injection time, ions accumulated for all parallisable time in centroid mode. MS3: in Synchronous Precursor Selection mode the top 10 MS2 ions were selected for HCD fragmentation (NCE 65) and scanned out in the Orbitrap at 50,000 resolution with an AGC target of $5x10^4$ and a maximum accumulation time of 150 ms, ions were not accumulated for all parallelisable time. The entire MS/MS/MS cycle had a target time of 3 s. Dynamic exclusion was set to +/- 10 ppm for 90 s. MS2 fragmentation was trigged on precursors $5x10^3$ counts and above.

Overview of MS measurement time requirements

Labelling method	MS protocol	Subcellular fractions/ map	Peptide fractions	Total samples for MS	MS run time/fraction (hours)	Total MS run time/map
SILAC	Fast	5	1	5	2.5	12.5
	Deep	5	3	15	2.5	37.5
LFQ5	Fast	5	1	5	2.5	12.5
	Deep	5	3	15	2.5	37.5
LFQ6	Fast	6	1	6	2.5	15
	Deep	6	3	18	2.5	45
TMT	Fast	5	1	1	3	1.5**
	Deep	5	12+1*	13	3	19.5**

* For TMT deep maps, the 12 peptide fractions were jointly processed with the single file from the corresponding fast map.

**TMT 10-plex allows running of two maps in one sample; hence, total MS run time is shown as half the actual run time.

Processing of mass spectrometry data

Raw files were processed with MaxQuant Version 1.5.5.2 (Cox and Mann, 2008; Tyanova et al., 2016a), using the human reference protein dataset downloaded from UniProt (SwissProt canonical and isoforms database). Default settings were used for all analyses, with the following exceptions:

For SILAC samples, multiplicity was set to 2, with Arg10 and Lys8 as heavy isotopes. The minimum ratio count was set to 1. Re-quantification was enabled. Matching between runs was enabled, to allow matching between equivalent fractions of replicates only.

For unlabelled samples, LFQ quantification (Cox et al., 2014) was selected, with a minimum peptide count of 1. Matching between equivalent fractions was enabled, as for SILAC samples.

For SILAC samples processed to simulate a label free experiment, multiplicity was set to 1 (SILAC light channel detected only). Matching between equivalent fractions was enabled. Please note that this procedure will underestimate the performance of LFQ dynamic maps, since a large proportion of the MS^2 peptide sequencing will be performed on SILAC heavy peptides, which do not contribute the quantification of the light peptides. This substantially reduces the sequencing depth and oversampling rate compared to a genuine single channel MS analysis; peptide IDs are reduced by about 30-40%.

For TMT labelled samples, batch-specific correction factors were configured in the modifications tab in MaxQuant (TMT 10-plex lot no. QK226224). Sample type was set to ‘reporter ion MS3’ with all 10-plex TMT labels selected, for both Lysine and N-termini. Matching between fractions was not activated. For deep TMT maps, the 12 fractions obtained with high pH fractionation were processed jointly with the single fraction from the corresponding fast map. In replicate 2, a contaminant of unknown origin reduced the MS performance; hence, all 24 high pH fractions and the single fast map file were jointly analysed. Nevertheless, the performance of replicate 2 remained substantially lower (4959 complete profiles). The depth we report for replicates 1 and 3 (6059 and 6699 profiles, respectively), obtained with 12+1 fractions, is therefore likely to be representative of the performance.

For mouse neuron data, raw files were processed with MaxQuant Version 1.5.4.3 (Cox and Mann, 2008; Tyanova et al., 2016a), using the mouse reference protein dataset downloaded from UniProt (SwissProt canonical and isoforms database). Default settings were used for all analyses, with the following exceptions: LFQ quantification (Cox et al., 2014) was selected, with a minimum peptide count of 1. Since the mouse neuron maps were prepared in three batches (one map in batch 1, two maps each in batches 2 and 3), matching between runs was enabled for equivalent and adjacent fractions within each batch only.

Filtering and transformation of proteomic data

The primary output from MaxQuant is the 'protein groups' file, listing protein identifications and the quantifications across the (five or six) subfractions. For all datasets, matches to the reverse database, proteins identified only with modified peptides, and common contaminants were removed. Further filtering was tailored to each labelling strategy, to obtain high quality datasets for further analysis.

For SILAC, profile filtering was always performed at the level of individual maps. Each map consisted of five ratio quantifications. For each fraction, SILAC ratios were linearly normalized by division through the fraction median. Individual ratios were retained if they were based on more than two quantification events, or on two quantification events where the ratio variability did not exceed 31%. Only proteins with a complete set of five ratios were retained. These SILAC ratio profiles were used for organellar assignments (SVM predictions, see below). For a direct comparison of SILAC profiles with TMT and LFQ profiles, further (0 to 1) normalization of profiles was required. For each protein, inverted SILAC ratios (Light/Heavy) were divided buy their sum.

For static LFQ maps, profile filtering was performed at the level of individual maps. Each map consisted of six fractions with LFQ intensities. MaxLFQ intensities are already globally normalized, and need no further normalization correction. Owing to the high dynamic range of label-free quantification, profiles with some missing values could be tolerated. Two stringency filters were applied: first, only proteins with LFQ intensities in at least three out of the six fractions were retained; and second, the MS/MS count summed over all six fractions had to be at least 12 (i.e. two per fraction on average). For each protein, LFQ intensities were normalized to the sum of LFQ intensities across the six fractions, yielding a six-data point profile of relative intensities (summing to one). These profiles were used for the generation of 6-fraction LFQ organellar maps.

To evaluate the performance of 5 fraction LFQ maps, the 1K fraction was removed from the dataset, and the remaining five data points were re-normalised to their sum. Thus, 5 and 6 fraction LFQ maps contain the exact same sets of proteins, permitting a fair comparison of the contribution made by the sixth fraction.

For dynamic LFQ maps (based on reprocessed SILAC data), only 5-data point profiles were available. These were filtered for a minimum of four consecutive LFQ values per protein and map. The dynamic LFQ experiment consisted of six maps (three controls and three +EGF treatment). For determining the MS/MS counts filter, MS/MS events were summed across all six maps (i.e. across 30 fractions). Only proteins with 60 or more MS/MS events in total were retained in the dataset. This alternative filtering strategy greatly enhances the scope of the MR plot translocation analysis, as it allows the inclusion of proteins that are abundant under one of the tested conditions, but not the other.

Each TMT labelled map consisted of five fractions with corrected reporter intensities. To account for unequal peptide loading in each fraction, a set of correction factors were determined by calculating the total intensity of each fraction divided by the fraction with the lowest summed intensity. Each value in a fraction was then divided by its own correction factor. Each TMT 10-plex experiment contained two maps, but these were treated separately for normalisation. For static TMT maps, proteins with a minimum median reporter intensity count of 1 across the five fractions were retained. For each protein, TMT intensities were then normalized to the sum of intensities within a map, yielding a five-data point profile (summing to one).

For dynamic TMT maps, this filtering was applied per experiment (i.e. the minimum median intensity count had to be 1 across ten fractions). As with the dynamic LFQ maps, this enhances the depth of the MR plot analysis.

Please note that for dynamic SILAC, TMT and LFQ maps, profiles were weighted with fraction yields (percent of protein recovered in a given subcellular fraction, relative to total yield) prior to 0-1 normalisation (Itzhak et al., 2016). While this step is recommended, it is not absolutely required.

Datasets for organellar predictions

To evaluate the suitability of different labelling strategies for making static organellar maps, performance was assessed at the level of individual maps, as well as for combinations of multiple maps.

To combine maps for classification, the set of proteins common to all maps was determined. Combining maps reduces the depth compared to the individual maps, but enhances classification accuracy. Support vector machine based classification (see below) was then performed on the total data available for each protein (e.g. 15 data points for a combination of 3 SILAC maps), resulting in one set of organellar prediction scores (regardless of how many maps were combined).

For LFQ, six individual fast maps were generated and assessed individually. The two lowest performing maps were then combined, for a joint output, followed by adding the third-lowest performing map and so on, up to a combination of all six maps. In all cases, only the proteins common to all six datasets were analysed.

An equivalent analysis was then repeated with three deep LFQ maps. These maps were generated from the same samples used for three of the fast maps, but with much more extensive MS analysis.

For SILAC, three fast maps and three deep maps were analysed likewise.

The TMT data had a different structure, as the 10-plexing allowed the concomitant generation of two (2 x 5 fraction) maps in one sample. Here, a control map was always multiplexed with its cognate EGF treatment map. For the evaluation of TMT static map performance, only fractions of the control map were processed as standard (five fraction) maps. Thus, three fast and three deep (untreated) TMT maps were analysed.

Based on the analysis presented in this study, we recommend the generation of three replicate maps, both for static and dynamic applications. Hence, map performance of all labelling approaches and MS protocols (fast vs deep) was compared for a combination of three maps (Figure 2, Figure 4, Figure S1). For LFQ fast analysis, we selected three medium performing maps from our set of six available maps, and jointly reprocessed them in MaxQuant. To combine maps, only proteins with high quality profiles in each map were selected for making organellar predictions. These six combination datasets were then assessed for prediction performance, depth, and concordance.

Organellar marker sets

For map annotation and supervised learning, we used our previously published set of 1,076 organellar markers from 12 different subcellular compartments (Itzhak et al., 2016). For SILAC (deep), TMT (deep), LFQ (deep) and LFQ (fast) maps, sets of around 1,000 markers were matched in each case. For SILAC (fast) and TMT (fast) analyses, map depth was considerably lower, and only 801 and 572 markers were matched, respectively. The minimum size for a cluster was seven members. In the case of TMT (fast), two clusters were too small, and hence excluded from the supervised learning.

For the mouse neuron maps the same set was used, matching markers by gene names (834 proteins matched).

Generation of organellar maps

For organellar assignments, we used the machine learning approach described in Itzhak et al. (2016), as implemented in Perseus software (Tyanova et al., 2016b). Briefly, organellar makers were matched to each map. A support vector machine (SVM)-algorithm (with a radial basis function kernel) was trained on the marker proteins, with cross-validation to prevent overfitting. Supervised learning was then performed with the optimized parameters, using full (leave-one-out) cross-validation for performance assessment.

The analysis provides two outputs: firstly, a misclassification table (or ‘confusion matrix’), listing which marker proteins had been assigned (correctly or incorrectly) to which compartment; and secondly, a prediction table, in which proteins receive prediction scores for each of the 12 compartments. Each protein is then assigned to the compartment for which it received the highest score. The sum of all these organellar assignments constitutes an organellar map.

Prediction scores are a measure of how confidently a protein is assigned to a compartment. Classification by SVMs defines (non-linear) maximum-margin boundaries between clusters; the distance from a cluster to the boundary is set to 1. Predictions with scores >1 therefore fall within the space defined by the markers; predictions with scores between 0 and 1 fall between the marker cluster and the boundary to markers from other clusters; and predictions with scores <0 are beyond the boundary. A prediction with a score <0 can still be correct, but less likely so. We therefore stratified our predictions into four confidence classes:

Prediction confidence classes

SVM score	Confidence	Class
>1	High	1
0.5-1	Medium	2
0-0.5	Low	3
<0	Very Low	4

Please note that in our previous study (Itzhak et al., 2016), we used a more complex scoring system, since the complete output from six individual maps was combined (and not just the overlapping set). For single maps, or for a combination of maps using the overlapping set of proteins as in the present study, this new scheme is recommended, as it allows a more straightforward interpretation of the scores and confidence classes, and is also directly comparable between sets of maps.

Performance evaluation of organellar maps

A pre-defined set of ca. 1000 bona fide markers of 12 different subcellular localisations/organelles (Itzhak et al., eLife 2016) was used to annotate any new map dataset. Support vector machines were optimized with the marker proteins, to define boundaries between the organellar clusters (see above, Generation of organellar maps). The quality of the final SVM model was evaluated with full leave-one-out cross validation (eg when there were 1000 marker proteins, 1000 different SVM models were built, each with only 999 proteins; in each case it was checked if the missing protein was correctly predicted, to simulate the application of the model to non-marker data). The average proportion of correctly predicted marker proteins was then assessed, both globally, and by cluster. This serves as an estimate of the prediction accuracy for the remainder of the data, which are not marker proteins.

The following metrics were calculated to assess map performance:

1. Marker prediction accuracy was calculated as the fraction of all correctly predicted markers divided by the total number of markers in the set. This metric gives more weight to larger protein clusters (such as mitochondria, plasma membrane and ER), whose prediction accuracy will dominate the global accuracy.
2. To evaluate the prediction performance for individual clusters, we calculated recall and precision. Recall is the proportion of markers correctly assigned to this cluster (i.e. True Positives/(True Positives + False Negatives)). Precision is the number of markers correctly assigned to a cluster, relative to the number of all markers assigned to the cluster (i.e. True Positives/ (True Positives + False Positives). Both metrics can be combined into an 'F1 score' by calculating their harmonic mean. F1 Scores range from 0-1. Unless both metrics have the same value, the harmonic mean is always lower than the arithmetic mean, thus ensuring that only combinations of high precision and recall values can achieve high F1 scores. For example, a cluster with perfect precision (1) but poor recall (0.2) would get a low F1 score of 0.33. Plotting F1 scores for all map clusters (as in Figure 2G) reveals particular strengths and weaknesses of a map; in our experience, clusters with scores >0.7 have high predictive value. Please note that F1 scores are not a linear measure of performance; for example, a near perfect cluster with precision and recall of 0.99 (almost no erroneous assignments, and almost complete coverage) would get a score of 0.99; a cluster with recall and precision of 0.5 (which misses half the real associations, and half of its assignments are incorrect) would get a score of 0.5. Although the score difference is less than two-fold, the performance difference is enormous.
3. To derive an overall map performance measure that weights each cluster equally, the average F1 score across the 12 clusters was calculated.

Furthermore, map depth, and the distribution of predictions into confidence classes (prediction stratification) were also evaluated. Map depth is the total number of proteins that passed the quality filters to be included for organellar predictions. For prediction stratification, marker proteins were removed from the set (since markers are used to build the SVM models, they generally have high SVM scores). Non-maker proteins were then sorted into the four prediction confidence classes (see above). The absolute number as well as the proportion of predictions in each class were scored (e.g. Figure 2I, J). Furthermore, overall marker prediction accuracy was

calculated within each confidence class; this varies between maps and methods (e.g. Figure 2H), and may suggest which predictions to include in a high confidence set. As a rule of thumb, predictions in the first two confidence classes are of high quality; hence, the greater the proportion of data in these classes, the better.

Concordance analysis

Map concordance ('agreement') was defined as the proportion of identical organellar assignments made by two independent maps. The joint outputs from three replicate maps (the 'combination data sets') provided by the different labelling methods were analysed. In all cases, predictions were compared to the output from SILAC deep maps (the most accurate in the set). Importantly, marker proteins were removed prior to the analysis; since they are very likely to have similar predictions across maps, their inclusion could otherwise skew the results.

First, the overlapping set of proteins between the SILAC Deep map and the compared map was determined. Second, the fraction of proteins with identical predictions in both maps, divided by the total number of proteins in the common set, was calculated. This provided the baseline concordance, using 100% of the overlapping data. Third, a quality filter on the predictions was introduced. Each organellar assignment is made with a confidence score (the higher, the better). Predictions made with low confidence scores are also less likely to be concordant between maps. For each protein, the lower of the two prediction scores was determined; map concordance was then calculated as a function of this minimum prediction score. By raising the cut-off, a growing proportion of data is excluded from the comparison, but concordance increases.

A corollary of the concordance analysis was that for all map types, regardless of depth and labelling strategy, predictions with scores >0.5 were highly concordant (typically >95-98%), and with scores >1 extremely concordant (typically >98-99.5%). These score cut-offs also coincide with the first two prediction confidence classes defined above.

Detection of dynamic changes between organellar maps

The detection of protein translocations mostly follows the procedure established in Itzhak et al., 2016, which is briefly recapitulated here. Adaptations for the LFQ and TMT workflows are detailed, as well as several modifications to improve the overall sensitivity and robustness of the test.

Datasets

The dynamic experiment consisted of three control samples, and three cognate samples from HeLa cells treated continuously with EGF for 20 min (Itzhak et al., 2016). The six maps obtained with each labelling strategy were analysed as sets.

Calculation of difference profiles

For each map pair, the normalized profile of the treated map was subtracted from the profile of the cognate control map. Three (5 data point) difference profiles were thus obtained for each protein.

Detection of proteins that move significantly between maps (MR plot analysis)

Differences between maps have two sources: genuine translocations of proteins, and experimental noise. Since most proteins do not move between conditions, the majority of difference profiles approximately follows a multivariate normal distribution. Genuine translocations are detected as multivariate outliers from this distribution. A standard statistical measure to define such outliers is the Mahalanobis distance. Since the latter's calculation is influenced by the outliers themselves, we used a robust calculation of the distance (the minimum covariance determinant, MCD). Distances follow a Chi-square distribution, which allows the conversion into p-values of likelihood for observing the measured distance by chance. The MCD outlier test is implemented in Perseus software (Tyanova et al., 2016b). A critical parameter for the MCD calculation is the proportion of data to use; whereas previously we have used 0.9, we now recommend 0.75, to increase sensitivity and robustness. Furthermore, the MCD derived p-values can be influenced by which proteins are chosen for the first-round calculations of this iterative process; hence, we recommend to calculate median p-values from at least 11

repeats, to ensure robust scores. A future version of Perseus will allow users to specify the number of iterations; we routinely run 101.

For each protein, the differences from three map pairs provide three p-values for movement. A genuine translocation should have a low p-value in each replicate experiment. To combine the replicates, we recommend choosing the highest of the three p-values. This represents the map pair with the smallest observed change. Since all three map pairs are independent experiments, this p-value is now cubed. The new combined p-value is then adjusted for multiple hypothesis correction using the Benjamini-Hochberg method (rank all p values from lowest to highest, multiply each value by the total number of proteins in the set, and divide it by its rank). This final Q-value is then -log(10) transformed, to obtain M (movement) scores. This modified procedure substantially enhances the sensitivity of outlier detection relative to the previous implementation; in addition, M scores now have directly interpretable meaning (e.g. an M score of 2 is equivalent to a Q-score of 0.01, i.e. a 1:100 FDR for movement detection of proteins with M scores of 2 or more). In the absence of proper FDR control datasets (see below), we recommend the following M scores cut offs: 2 (lenient), 3 (stringent), 4 (very stringent).

Genuine translocations have consistent directions across replicates, and hence similar map difference profiles. As a measure of translocation reproducibility, the Pearson correlation of all pairs of difference profiles (Rep1 vs Rep2, Rep1 vs Rep3, Rep2 vs Rep3) is calculated. The lowest correlation is then chosen as the R (reproducibility) score. Only translocations with highly (positively) correlated profile changes are of interest. In the absence of proper FDR control datasets, we recommend the following R-score cut-offs: 0.68 (lenient), 0.81 (stringent), 0.93 (very stringent).

Please note that R scores are orthogonal to M-scores. Their combination ('MR' plot analysis as in Figure 3) results in very strict filtering, even with 'lenient' M and R score cut-offs.

False discovery rate (FDR) control of MR plot analyses

As described previously (Itzhak et al., 2016), the best way to determine significance cut-offs for a MR plot analysis is to perform a mock experiment (three control maps vs three cognate control maps). No genuine translocations are expected under these conditions. The MR plot analysis is performed as described above. Cut-offs for M and R scores are then simultaneously applied to both mock and treatment datasets, and the number of significant movers in the mock set divided by the number found in the treatment experiment corresponds to the estimated FDR at a given MR score cut off. Cut-offs may then be selected to achieve a desired FDR (e.g. 10%, or 1%); alternatively, the FDR at a desired MR cut-off combination may be calculated.

In the present study, the SILAC and LFQ (fast and deep) analyses were fully FDR controlled. The mock dataset for SILAC was provided by the six SILAC (deep) control maps reported in Itzhak et al. (2016). For LFQ, these SILAC maps were reprocessed using the MaxLFQ algorithm (ignoring the SILAC heavy peptides). In all cases, the number of significant hits in the mock set was scaled by the number of profiled proteins in mock and treatment sets. For TMT data, no FDR control dataset was available. As a proxy, we used the same MR cut-offs chosen for the LFQ and SILAC sets.

Profile scatter analysis

Profile scatter within the 20S core proteasome (14 subunits, PSMA1-7, PSMB1-7) was analysed. Only the profiles from the 'deep' combination datasets (with three biological replicates) were included. For each method, the 3 x 14 (0-1 normalised) profiles were extracted, and the 'average' profiles of each replicate determined. Summed absolute deviations from these averages (Manhattan Distances) were then calculated for each subunit, within each replicate. The scatter of the 42 differences was then plotted.

Principal component analysis

For graphical map representation, weighted normalised profiles of the 941 marker proteins common to the SILAC, LFQ and TMT combination datasets (3 deep maps each) were scaled to unit variance, and jointly subjected to principal component analysis (PCA). Figure 4 shows the projections along PCs 1 and 2 (scores plot). For the LFQ6 dataset, a separate PCA had to be performed, since it had one extra fraction per map. To allow optimum visual comparison, the same region of the LFQ6 scores plot is shown as for the other maps, causing clipping of 48 large protein complex markers outside this region.

Software for statistical analysis and graphics

Statistical analyses, data transformation and filtering were performed in Perseus (Tyanova et al., 2016b), Prism 6 (GraphPad Software), and Microsoft Excel (enhanced with the Real Statistics Resource Pack, http://www.real-statistics.com). Principal component analysis was performed in SIMCA 14 (Umetrics/MKS).

Webpage www.MapOfTheCell.org

We have improved the web interface for our database of human subcellular localization predictions.

Mouse neuron organellar anatomy analysis

Copy number determination

Copy numbers per cell, protein concentrations and cell volumes were estimated with the proteomic ruler approach (Wisniewski et al., 2014), implemented in Perseus software (Tyanova et al., 2016b). Briefly, mass spectrometric protein intensities are scaled to the summed histone intensities. Since the histone to DNA ratio is relatively constant, and the amount of DNA per cell is known, the total histone signal can be converted into an absolute protein quantity per cell. All other protein intensities can be scaled accordingly. Normalization to protein molecular weight then yields copy numbers per cell. Based on an estimated total cellular protein concentration of 200 mg/ml, the method also allows an approximate estimation of cell volume, and hence of protein concentrations (Wisniewski et al., 2014).

The proteomic ruler approach requires determination of a complete proteome as input. For the mouse neurons, we derived this in two different ways. First, we used the conventional approach, and directly processed a sample of whole cell lysates for mass spectrometric analysis ('fast' MS protocol, one sample per proteome). This resulted in a depth of ca. 6,000 quantified proteins (from biological duplicates). As an alternative, we combined the mass spectrometric analyses from all seven fractions from organellar map experiments (Figure 5A); the sum of these fractions corresponds to the total cell content. Mass spectrometric intensities from each fraction were normalized to the sum total, and weighted by relative fraction yields as determined by BCA protein assay. Weighted intensities were then added to derive total intensities for each protein. This resulted in a depth of ca. 9,000 quantified proteins (from biological quadruplicates, preps 2-5). The proteomic ruler was then applied to both datasets ('standard' proteome and 'compound' proteome). Importantly, copy number estimates of proteins identified with both methods were highly consistent (correlation >0.95, slope near 1; Figure S3A). Furthermore, both datasets showed the same expected log-normal distribution, with an extended lower range for the compound full proteome (Figure S3B, C). Hence, it is valid to use the compound proteome for copy numbers. The advantage is that the compound proteome is derived from samples that are already analysed as part of the organellar mapping process; no extra samples are required. The depth is also increased, owing to the cell fractionation. We hence recommend this approach for applications where starting material and/or mass spectrometric measuring time are limited.

For the proteomic ruler analysis, we assumed a ploidy of two for mouse neurons, and normalized intensities by protein molecular weight. All proteomes were normalized separately. Default settings were used for all other parameters. Copy numbers and concentrations were calculated as median values from replicates (in log space).

Global protein distribution analysis

To determine the global distribution of proteins ('low resolution' spatial information), we quantified their abundance in the nuclear, cytosolic and membrane fractions (Figure 5A), similar to our previous analysis in HeLa cells (see Itzhak et al., 2016, for details). Briefly, intensities in each fraction were normalized to the sum total, and weighted by their relative yields (as determined by BCA protein assay). Intensities from membrane fractions (2-6 in Figure 5A) were then combined (total membrane fraction). Intensities in the nuclear, cytosolic or membrane fractions were then summed, and expressed as fractions of 1. Proteins were then classified based on their distribution using arbitrary cut-offs:

Classifier	Distribution
Mostly nuclear	nuclear pool >0.9
Mostly membrane associated	membrane pool >0.8
Mostly cytosolic	cytosolic pool >0.9
Nuclear and Cytosolic	(nuclear + cytosolic pools) >0.95
Membrane associated with cytosolic pool	(membrane +cytosolic pools) >0.95
Unclassified	all other proteins

Please note that some proteins had a global as well as an organellar classifier; in these cases, the organellar classifier describes where the membrane associated pool of the protein is located, and the global classifier reports the cytosolic and/or nuclear proportion of the protein.

Mouse neuron organellar composition analysis

Subcellular localization predictions and copy number information were combined to derive organellar compositions, as described (Itzhak et al., 2016). For each organelle, a list of predicted constituents (Table S4) was prepared. For each protein, the copy number/cell was multiplied with the protein's molecular weight, to obtain the total protein mass/cell. Next, this mass was multiplied by the non-cytosolic fraction of the protein. All weighted masses were summed, to obtain the total protein mass of the organelle (per cell). Each protein's contribution to the organelle's total mass was then expressed as a percentage. Dividing the whole organellar protein mass by the whole cell protein mass yielded the relative contribution of the organelle to the cell.

Since lysis of cells invariably causes disruption of ER and thus exaggerated apparent cytosolic pools of ER lumenal proteins (Itzhak et al., 2016), the non-cytosolic correction factor was set to 1 for ER; this was also done for lysosomal proteins, which are mostly lumenal or integral to the membrane.

Comparative analysis mouse neurons vs HeLa

For a quantitative comparison of cell anatomy, we compared the mouse neuron data of this study with our previously prepared HeLa data (Itzhak et al., 2016). We matched identified proteins by UniProt gene name (which is identical between human and mouse in most cases), and assumed that such matched proteins represent orthologues. We also removed duplicated entries for the same gene name within one organism (eg splice variants of the same protein), keeping only the most abundant entry. After filtering, our proteomes contained 8601 and 8469 proteins for mouse neurons and HeLa, respectively. The complete proteome of both cell types is estimated at >10,000 proteins. However, as our plateauing cumulative abundance analysis shows (Figure 6B), the 'missing' proteins are likely to contribute minimally to overall cell protein mass, and hence will not substantially affect the quantitative composition analysis.

Comparisons were performed at the full proteome and organellar levels. 6,708 proteins were identified in neurons and HeLa; hence 78% (6,708/8,601) of the neuron proteome is shared with HeLa cells. For calculating the protein mass overlap, the respective contributions of each shared protein to total proteins mass were compared; the lower value was chose as the overlap. The summed overlap yielded the overall shared mass. To assess organellar composition overlap, the top ten most abundant proteins from each neuron organelle were matched to their HeLa cell orthologues. For each protein, the respective contributions to total neuron or HeLa compartment protein mass were then compared.

Supplemental References

Akimov, V., Rigbolt, K.T., Nielsen, M.M., and Blagoev, B. (2011). Characterization of ubiquitination dependent dynamics in growth factor receptor signaling by quantitative proteomics. Mol Biosyst *7*, 3223-3233.

Arimoto, K., Burkart, C., Yan, M., Ran, D., Weng, S., and Zhang, D.E. (2014). Plakophilin-2 promotes tumor development by enhancing ligand-dependent and -independent epidermal growth factor receptor dimerization and activation. Mol Cell Biol *34*, 3843-3854.

Bryk, A.H., and Wisniewski, J.R. (2017). Quantitative Analysis of Human Red Blood Cell Proteome. J Proteome Res 16, 2752-2761.

Eskova, A., Knapp, B., Matelska, D., Reusing, S., Arjonen, A., Lisauskas, T., Pepperkok, R., Russell, R., Eils, R., Ivaska, J., *et al.* (2014). An RNAi screen identifies KIF15 as a novel regulator of the endocytic trafficking of integrin. J Cell Sci *127*, 2433-2447.

Fan, Q.W., Cheng, C., Knight, Z.A., Haas-Kogan, D., Stokoe, D., James, C.D., McCormick, F., Shokat, K.M., and Weiss, W.A. (2009). EGFR signals to mTOR through PKC and independently of Akt in glioma. Sci Signal *2*, ra4.

Fang, Z., Takizawa, N., Wilson, K.A., Smith, T.C., Delprato, A., Davidson, M.W., Lambright, D.G., and Luna, E.J. (2010). The membrane-associated protein, supervillin, accelerates F-actin-dependent rapid integrin recycling and cell motility. Traffic *11*, 782-799.

Fogelgren, B., Zuo, X., Buonato, J.M., Vasilyev, A., Baek, J.I., Choi, S.Y., Chacon-Heszele, M.F., Palmyre, A., Polgar, N., Drummond, I., *et al.* (2014). Exocyst Sec10 protects renal tubule cells from injury by EGFR/MAPK activation and effects on endocytosis. Am J Physiol Renal Physiol *307*, F1334-1341.

Fukata, Y., Oshiro, N., Kinoshita, N., Kawano, Y., Matsuoka, Y., Bennett, V., Matsuura, Y., and Kaibuchi, K. (1999). Phosphorylation of adducin by Rho-kinase plays a crucial role in cell motility. J Cell Biol *145*, 347-361.

Galovic, M., Xu, D., Areces, L.B., van der Kammen, R., and Innocenti, M. (2011). Interplay between N-WASP and CK2 optimizes clathrin-mediated endocytosis of EGFR. J Cell Sci *124*, 2001-2012.

He, W., Rose, D.W., Olefsky, J.M., and Gustafson, T.A. (1998). Grb10 interacts differentially with the insulin receptor, insulin-like growth factor I receptor, and epidermal growth factor receptor via the Grb10 Src homology 2 (SH2) domain and a second novel domain located between the pleckstrin homology and SH2 domains. J Biol Chem *273*, 6860-6867.

Holland, S., Coste, O., Zhang, D.D., Pierre, S.C., Geisslinger, G., and Scholich, K. (2011). The ubiquitin ligase MYCBP2 regulates transient receptor potential vanilloid receptor 1 (TRPV1) internalization through inhibition of p38 MAPK signaling. J Biol Chem *286*, 3671-3680.

Hosseinibarkooie, S., Peters, M., Torres-Benito, L., Rastetter, R.H., Hupperich, K., Hoffmann, A., Mendoza-Ferreira, N., Kaczmarek, A., Janzen, E., Milbradt, J., *et al.* (2016). The Power of Human Protective Modifiers: PLS3 and CORO1C Unravel Impaired Endocytosis in Spinal Muscular Atrophy and Rescue SMA Phenotype. Am J Hum Genet *99*, 647-665.

Hu, J., Troglio, F., Mukhopadhyay, A., Everingham, S., Kwok, E., Scita, G., and Craig, A.W. (2009). F-BAR-containing adaptor CIP4 localizes to early endosomes and regulates Epidermal Growth Factor Receptor trafficking and downregulation. Cell Signal *21*, 1686-1697.

Julian, L., and Olson, M.F. (2014). Rho-associated coiled-coil containing kinases (ROCK): structure, regulation, and functions. Small GTPases *5*, e29846.

Kamano, Y., Saeki, M., Egusa, H., Kakihara, Y., Houry, W.A., Yatani, H., and Kamisaki, Y. (2013). PIH1D1 interacts with mTOR complex 1 and enhances ribosome RNA transcription. FEBS Lett *587*, 3303-3308.

Karunagaran, D., Tzahar, E., Beerli, R.R., Chen, X., Graus-Porta, D., Ratzkin, B.J., Seger, R., Hynes, N.E., and Yarden, Y. (1996). ErbB-2 is a common auxiliary subunit of NDF and EGF receptors: implications for breast cancer. EMBO J *15*, 254-264.

Klessner, J.L., Desai, B.V., Amargo, E.V., Getsios, S., and Green, K.J. (2009). EGFR and ADAMs cooperate to regulate shedding and endocytic trafficking of the desmosomal cadherin desmoglein 2. Mol Biol Cell *20*, 328-337.

Kozik, P., Hodson, N.A., Sahlender, D.A., Simecek, N., Soromani, C., Wu, J., Collinson, L.M., and Robinson, M.S. (2013). A human genome-wide screen for regulators of clathrin-coated vesicle formation reveals an unexpected role for the V-ATPase. Nat Cell Biol *15*, 50-60.

Larsson, A.H., Lehn, S., Wangefjord, S., Karnevi, E., Kuteeva, E., Sundstrom, M., Nodin, B., Uhlen, M., Eberhard, J., Birgisson, H., *et al.* (2016). Significant association and synergistic adverse prognostic effect of podocalyxin-like protein and epidermal growth factor receptor expression in colorectal cancer. J Transl Med *14*, 128.

Lewis-Saravalli, S., Campbell, S., and Claing, A. (2013). ARF1 controls Rac1 signaling to regulate migration of MDA-MB-231 invasive breast cancer cells. Cell Signal *25*, 1813-1819.

Liu, K., Jiang, T., Ouyang, Y., Shi, Y., Zang, Y., Li, N., Lu, S., and Chen, D. (2015). Nuclear EGFR impairs ASPP2-p53 complex-induced apoptosis by inducing SOS1 expression in hepatocellular carcinoma. Oncotarget *6*, 16507-16516.

Lorch, J.H., Klessner, J., Park, J.K., Getsios, S., Wu, Y.L., Stack, M.S., and Green, K.J. (2004). Epidermal growth factor receptor inhibition promotes desmosome assembly and strengthens intercellular adhesion in squamous cell carcinoma cells. J Biol Chem *279*, 37191-37200.

Lowenstein, E.J., Daly, R.J., Batzer, A.G., Li, W., Margolis, B., Lammers, R., Ullrich, A., Skolnik, E.Y., Bar-Sagi, D., and Schlessinger, J. (1992). The SH2 and SH3 domain-containing protein GRB2 links receptor tyrosine kinases to ras signaling. Cell *70*, 431-442.

Mader, C.C., Oser, M., Magalhaes, M.A., Bravo-Cordero, J.J., Condeelis, J., Koleske, A.J., and Gil-Henn, H. (2011). An EGFR-Src-Arg-cortactin pathway mediates functional maturation of invadopodia and breast cancer cell invasion. Cancer Res *71*, 1730-1741.

Matsuhashi, S., Hamajima, H., Xia, J., Zhang, H., Mizuta, T., Anzai, K., and Ozaki, I. (2014). Control of a tumor suppressor PDCD4: Degradation mechanisms of the protein in hepatocellular carcinoma cells. Cell Signal *26*, 603-610.

Novellasdemunt, L., Tato, I., Navarro-Sabate, A., Ruiz-Meana, M., Mendez-Lucas, A., Perales, J.C., Garcia-Dorado, D., Ventura, F., Bartrons, R., and Rosa, J.L. (2013). Akt-dependent activation of the heart 6-phosphofructo-2-kinase/fructose-2,6-bisphosphatase (PFKFB2) isoenzyme by amino acids. J Biol Chem *288*, 10640-10651.

Pai, R., Szabo, I.L., Giap, A.Q., Kawanaka, H., and Tarnawski, A.S. (2001). Nonsteroidal anti-inflammatory drugs inhibit re-epithelialization of wounded gastric monolayers by interfering with actin, Src, FAK, and tensin signaling. Life Sci *69*, 3055-3071.

Sakaguchi, K., Okabayashi, Y., Kido, Y., Kimura, S., Matsumura, Y., Inushima, K., and Kasuga, M. (1998). Shc phosphotyrosine-binding domain dominantly interacts with epidermal growth factor receptors and mediates Ras activation in intact cells. Mol Endocrinol *12*, 536-543.

Schmandt, R., Liu, S.K., and McGlade, C.J. (1999). Cloning and characterization of mPAL, a novel Shc SH2 domain-binding protein expressed in proliferating cells. Oncogene *18*, 1867-1879.

Sherrill, J.M., and Kyte, J. (1996). Activation of epidermal growth factor receptor by epidermal growth factor. Biochemistry *35*, 5705-5718.

Soubeyran, P., Barac, A., Szymkiewicz, I., and Dikic, I. (2003). Cbl-ArgBP2 complex mediates ubiquitination and degradation of c-Abl. Biochem J *370*, 29-34.

Tong, J., Taylor, P., and Moran, M.F. (2014). Proteomic analysis of the epidermal growth factor receptor (EGFR) interactome and post-translational modifications associated with receptor endocytosis in response to EGF and stress. Mol Cell Proteomics *13*, 1644-1658.

Vincent, S., and Settleman, J. (1997). The PRK2 kinase is a potential effector target of both Rho and Rac GTPases and regulates actin cytoskeletal organization. Mol Cell Biol *17*, 2247-2256.

Wang, Y., Du, D., Fang, L., Yang, G., Zhang, C., Zeng, R., Ullrich, A., Lottspeich, F., and Chen, Z. (2006). Tyrosine phosphorylated Par3 regulates epithelial tight junction assembly promoted by EGFR signaling. EMBO J *25*, 5058-5070.

Watanuki, Z., Kosai, H., Osanai, N., Ogama, N., Mochizuki, M., Tamai, K., Yamaguchi, K., Satoh, K., Fukuhara, T., Maemondo, M., *et al.* (2014). Synergistic cytotoxicity of afatinib and cetuximab against EGFR T790M involves Rab11-dependent EGFR recycling. Biochem Biophys Res Commun *455*, 269-276.

Wheeler, M., and Domin, J. (2001). Recruitment of the class II phosphoinositide 3-kinase C2beta to the epidermal growth factor receptor: role of Grb2. Mol Cell Biol *21*, 6660-6667.

Xu, C.L., Wang, J.Z., Xia, X.P., Pan, C.W., Shao, X.X., Xia, S.L., Yang, S.X., and Zheng, B. (2016). Rab11-FIP2 promotes colorectal cancer migration and invasion by regulating PI3K/AKT/MMP7 signaling pathway. Biochem Biophys Res Commun *470*, 397-404.

Zhang, X., Belkina, N., Jacob, H.K., Maity, T., Biswas, R., Venugopalan, A., Shaw, P.G., Kim, M.S., Chaerkady, R., Pandey, A., *et al.* (2015). Identifying novel targets of oncogenic EGF receptor signaling in lung cancer through global phosphoproteomics. Proteomics *15*, 340-355.

Zhong, S., Yin, H., Liao, Y., Yao, F., Li, Q., Zhang, J., Jiao, H., Zhao, Y., Xu, D., Liu, S., *et al.* (2015). Lung Tumor Suppressor GPRC5A Binds EGFR and Restrains Its Effector Signaling. Cancer Res *75*, 1801-1814.